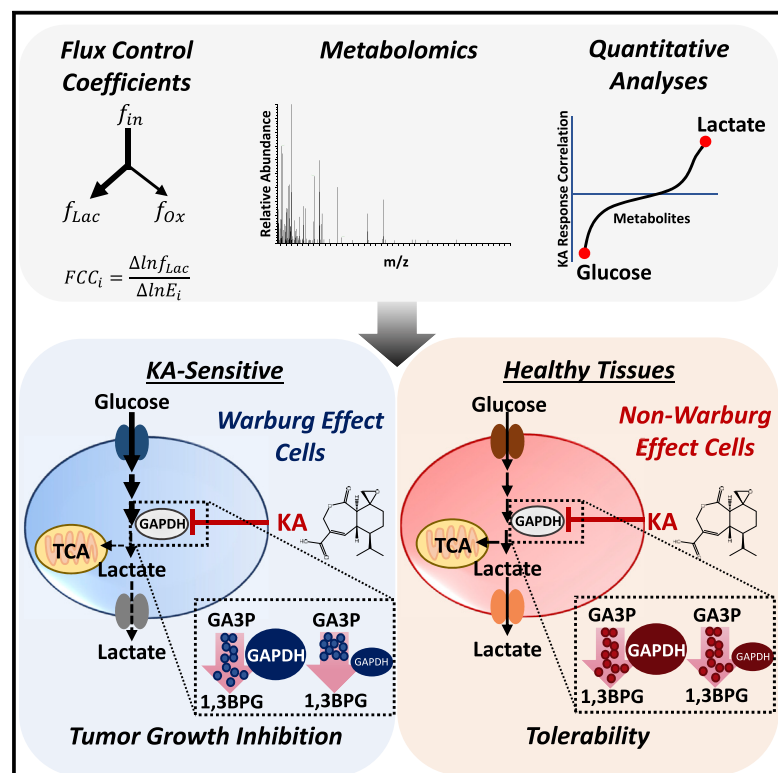# Cell Metabolism

A Predictive Model for Selective Targeting of the Warburg Effect through GAPDH Inhibition with a Natural Product

Graphical Abstract

Authors

Maria V. Liberti, Ziwei Dai, Suzanne E. Wardell, ..., Frank C. Schroeder, Donald P. McDonnell, Jason W. Locasale

Correspondence

jason.locasale@duke.edu

In Brief

Liberti et al. use metabolic control analysis and multi-omics approaches to show that the enzyme GAPDH is rate limiting for the Warburg effect in cancer cells. They identify a therapeutic window where partial GAPDH inhibition is more selective for highly glycolytic tumors, highlighting how metabolism is an integral part of precision medicine.

Highlights

- Flux control analysis reveals GAPDH as rate limiting during the Warburg effect (WE)

- Koningic acid (KA) is nominated and validated as a specific GAPDH inhibitor

- Machine learning shows that the quantitative extent of the WE predicts KA response

- Partial GAPDH inhibition is tolerable and selective for highly glycolytic tumors

CellPress

Article

CellPress

A Predictive Model for Selective Targeting of the Warburg Effect through GAPDH Inhibition with a Natural Product

Maria V. Liberti,[1,2] Ziwei Dai,[1] Suzanne E. Wardell,[1] Joshua A. Baccile,[3] Xiaojing Liu,[1] Xia Gao,[1] Robert Baldi,[1] Mahya Mehrmohamadi,[1,2] Marc O. Johnson,[4] Neel S. Madhukar,[5] Alexander A. Shestov,[6] Iok I. Christine Chio,[7] Olivier Elemento,[5] Jeffrey C. Rathmell,[4] Frank C. Schroeder,[3] Donald P. McDonnell,[1] and Jason W. Locasale[1,8,*]

[1]Department of Pharmacology and Cancer Biology, Duke Cancer Institute, Duke University School of Medicine, Durham, NC 27710, USA
[2]Department of Molecular Biology and Genetics
[3]Boyce Thompson Institute and Department of Chemistry and Chemical Biology
Cornell University, Ithaca, NY 14853, USA
[4]Department of Pathology, Microbiology, and Immunology, Vanderbilt Center for Immunobiology, Vanderbilt University Medical Center, Nashville, TN 37232, USA
[5]Department of Physiology and Biophysics, Meyer Cancer Center, Institute for Precision Medicine and Institute for Computational Biomedicine, Weill Cornell Medicine, New York, NY 10021, USA
[6]Molecular Imaging and Metabolomics Lab, Radiology Department, Perelman School of Medicine, University of Pennsylvania, Philadelphia, PA 19104, USA
[7]Cold Spring Harbor Laboratory, Lustgarten Foundation Pancreatic Cancer Research Laboratory, Cold Spring Harbor, NY 11724, USA
[8]Lead Contact
*Correspondence: jason.locasale@duke.edu
http://dx.doi.org/10.1016/j.cmet.2017.08.017

SUMMARY

Targeted cancer therapies that use genetics are successful, but principles for selectively targeting tumor metabolism that is also dependent on the environment remain unknown. We now show that differences in rate-controlling enzymes during the Warburg effect (WE), the most prominent hallmark of cancer cell metabolism, can be used to predict a response to targeting glucose metabolism. We establish a natural product, koningic acid (KA), to be a selective inhibitor of GAPDH, an enzyme we characterize to have differential control properties over metabolism during the WE. With machine learning and integrated pharmacogenomics and metabolomics, we demonstrate that KA efficacy is not determined by the status of individual genes, but by the quantitative extent of the WE, leading to a therapeutic window in vivo. Thus, the basis of targeting the WE can be encoded by molecular principles that extend beyond the status of individual genes.

INTRODUCTION

The general approach in cancer research is to define and then exploit the molecular requirements that distinguish tumor from normal. Targeted cancer therapies have used genomic alterations and differences in gene expression as biomarkers to predict therapeutic efficacy with great success. This strategy is currently the major paradigm within the current concept of precision medicine, with each one's disease having a specific molecular profile that determines the appropriate course of action (Collins and Varmus, 2015). In contrast, the determinants of therapies that target metabolism for the treatment of complex diseases, such as diabetes, do not depend on the status of a single gene because the principles that determine a specific response to alterations in metabolism are multifaceted convolutions of both genetic and environmental factors (Vander Heiden and DeBerardinis, 2017). Furthermore, predictive models for targeting cancer metabolism have not yet been successfully developed from the mutational or expression status of individual genes (Vander Heiden and DeBerardinis, 2017). Therefore, substantial challenges, especially regarding the appropriate populations that should be investigated, have limited advances in therapies that target cancer metabolism (Garber, 2016).

The most prominent hallmark of cancer metabolism is the Warburg effect (WE), or aerobic glycolysis, which is defined by the increased uptake of glucose and incomplete oxidation or fermentation to lactate in the presence of oxygen. The WE has been extensively studied over the years and is routinely exploited clinically as a diagnostic of tumor burden with predictive features of cancer outcome (Liberti and Locasale, 2016; Vander Heiden, 2013). There are a number of strategies that have been proposed to target the WE, including targeting oncogenes and tumor suppressor genes that interact with glucose metabolism and the specific isoforms of glycolytic enzymes that are expressed in cancer (Hay, 2016). However, full target inhibition, and thus complete ablation of an enzyme involved in metabolizing glucose, encounters limiting toxicity as glucose metabolism is required in nearly every mammalian tissue. Therefore, partial inhibition of glycolytic enzyme activity with selectivity against tumors is needed. Whether this specificity is possible and the strategy needed to define it are unknown.

An alternative approach to developing a predictive model for targeting cancer metabolism is to exploit differential properties
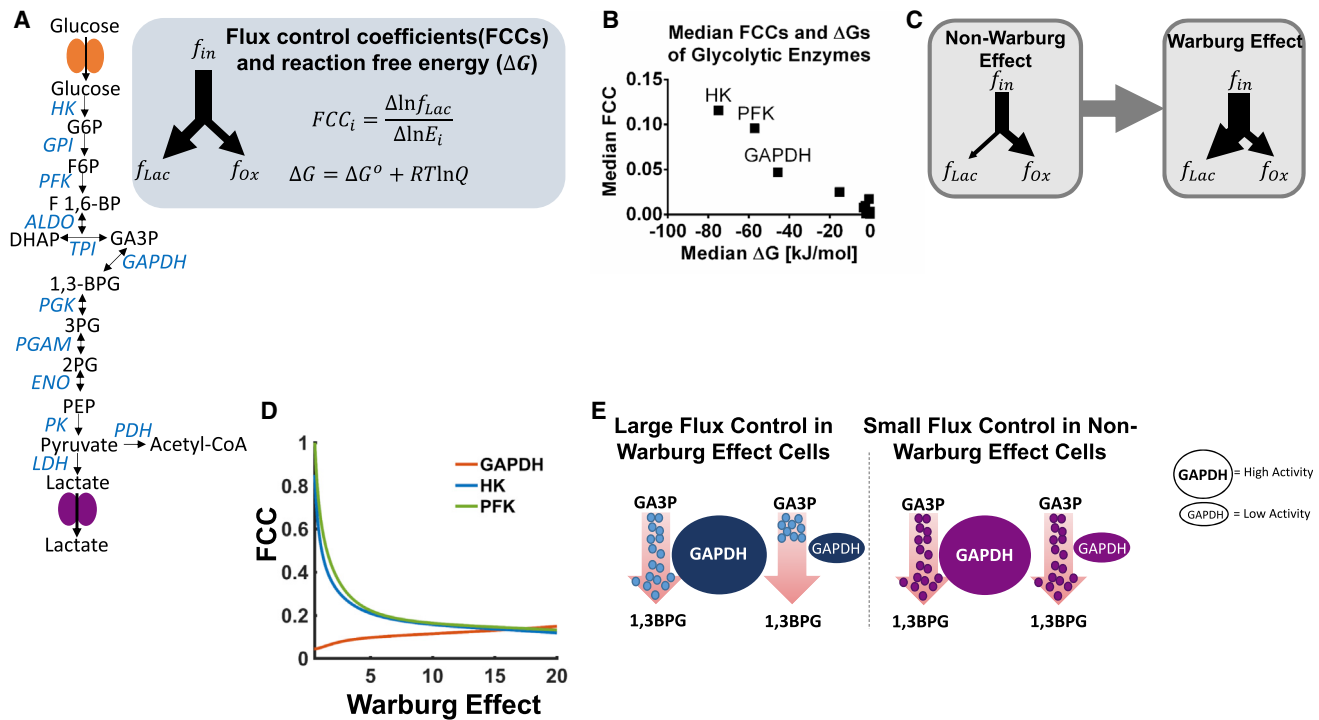
Figure 1. Thermodynamic and Kinetic Analysis of Rate Control in Glycolysis
(A) Glycolysis pathway with metabolites (black) and enzymes (blue). Model for flux control coefficients (FCCs) and reaction free energy (ΔG) values. f, flux.
(B) Median FCCs versus median ΔGs of glycolytic enzymes. HK, hexokinase; PFK, phosphofructokinase; GAPDH, glyceraldehyde-3-phosphate dehydrogenase.
(C) Schematic showing flux inputs and outputs during non-WE and WE conditions.
(D) Relationship between FCC values of GAPDH, HK, and PFK and extent of the WE defined as ratio of lactate production flux to oxidative phosphorylation flux.
(E) Schematic demonstrating the high rate-limiting effect of GAPDH over cells carrying out the WE compared to those undergoing oxidative phosphorylation. GA3P, glyceraldehyde-3-phosphate; 1,3-BPG, 1,3-bisphosphoglycerate.

of network activity (e.g., metabolic flux). In this scenario, the glycolytic pathway would be affected by a perturbation to one of its enzymes during conditions that promote the WE, and the same perturbation would leave glucose metabolism lesser affected in conditions of normal physiology. This concept of synthetic lethality has been developed in cancer biology by identifying genetic events that create liabilities, but a lesser-studied, if not novel approach to identify these vulnerabilities is to use the quantitative properties encoded in the kinetics and thermodynamics of the metabolic network that are different during the WE. It is known that the level of control that a metabolic enzyme exerts on a metabolic flux depends on properties other than the expression or activity of the given enzyme. Thus, a change in enzyme activity could result in a different effect on metabolic output depending on other properties of the metabolic network. To our knowledge, this concept has not been explored in cancer therapy.

There are generally thought to be three rate-controlling enzymes in glycolysis: hexokinase (HK), phosphofructokinase (PFK), and pyruvate kinase (Lehninger et al., 2013). However, metabolic control analysis (MCA) (Fell, 1992), a quantitative approach to evaluate the amount of enzyme activity that is required to alter the overall output of a pathway, has suggested that the rate control may be different during the WE (Shestov et al., 2014). Furthermore, MCA has proven invaluable in designing and controlling metabolic pathways for biotechnology

applications (Bowden, 1999), but has not, to our knowledge, been explored in biomedical settings. We therefore reasoned that MCA, by identifying differences in biochemical regulation occurring at the systems or network level of the glycolytic pathway (i.e., flux control), could allow for selective targeting of the WE, thus identifying predictors for therapeutic response that are encoded within metabolism. In the present study, we sought to test this hypothesis.

RESULTS

Thermodynamic and Kinetic Analysis of Rate Control in Glycolysis

Based on our previously published mathematical model of glycolysis (Shestov et al., 2014), we performed MCA (Heinrich and Schuster, 1996) on lactate production flux and evaluated thermodynamics for each step in glycolysis by calculating flux control coefficients (FCCs) and reaction-free energies (ΔGs) (Figure 1A). While these models have limitations due to our incomplete knowledge of glycolysis, they can allow for discovery with further appropriate validation. Steps with higher FCCs and lower ΔGs are known to exert stronger control over flux through the pathway (Noor et al., 2014). We compared the FCCs of each enzymatic step in glycolysis to their ΔGs (Figure 1B). Two of the canonical rate-limiting enzymes of glycolysis, HK and PFK, exhibited high FCCs and low ΔGs as expected. However, a third

CellPress
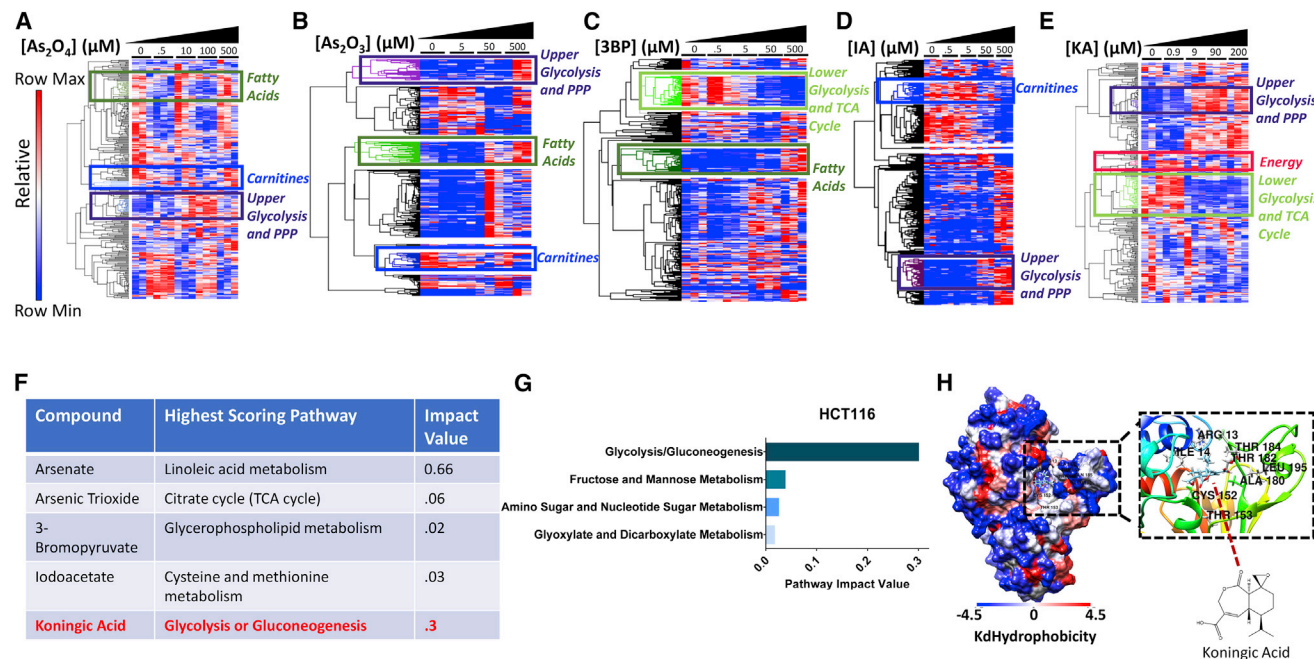
Figure 2. Comparative Metabolomics Nominates a Specific GAPDH Inhibitor

(A–E) Clustered heatmaps with pathway and dose annotations of dose-dependent global metabolic responses to putative GAPDH inhibitors.

(A) Arsenate (As_2O_4).

(B) Arsenic trioxide (As_2O_3).

(C) 3-bromopyruvate (3BP).

(D) Iodoacetate (IA).

(E) Koningic acid (KA).

(F) Network-based pathway analysis for each compound.

(G) Pathway analysis showing top four highest scoring pathways in response to KA.

(H) KA docking analysis to GAPDH active site Cys152.

glycolytic enzyme, glyceraldehyde-3-phosphate dehydrogenase (GAPDH), also displayed a high FCC and low ΔG, indicating that GAPDH also may be a rate-controlling enzyme of glycolysis in some settings.

To study the relationship between the WE and control of glycolysis, we tuned the model to exhibit varying extents of the WE by altering activities of glycolytic enzymes with the highest variation in protein abundance (Figure 1C). Although HK, PFK, and GAPDH all exhibit considerable control over flux in glycolysis, only the value of GAPDH FCC increases during the WE (Figure 1D). Therefore, inhibiting GAPDH activity exerts larger reduction in glycolytic flux in cells undergoing a higher degree of the WE than in cells with lower glycolytic activity (Figure 1E), thus providing a rationale for exploring the control of glycolytic rate by GAPDH as a target against the WE.

Comparative Metabolomics Nominates a Specific GAPDH Inhibitor

We next evaluated the cytotoxic activities of several putative GAPDH inhibitors, including arsenate, arsenic trioxide, 3-bromopyruvate, iodoacetate, and koningic acid (KA) (Campbell-Burk et al., 1987; Dai et al., 1999; Endo et al., 1985; Ganapathy-Kanniappan et al., 2009; Németi and Gregus, 2005), and found substantial variability (Figure S1A), indicating that they have different pharmacological activities and possibly act by different mecha-

nisms. To further investigate this likely possibility, we generated dose-dependent metabolite profiles in HCT116 cells comprising over 350 metabolites and found that each profile exhibited differences in the levels of glycolytic metabolites and related pathways (Figures 2A–2E). However, with the exception of KA, all other profiles exhibited many other perturbations to metabolism as well. These effects were quantified using a network-based pathway analysis (STAR Methods) that revealed glycolysis as the highest scoring pathway only in KA-treated cells (Figures 2F and 2G). Consistent with this finding, a docking analysis indicates that KA can directly bind to the active site of human GAPDH (Figure 2H).

At the concentration corresponding to the IC_{50} value of KA (Figure S1A), GAPDH activity decreased compared to vehicle (Figure S1B). To examine how KA-induced decreases in GAPDH activity exert cytotoxic effects, we evaluated the response at the IC_{50} using a volcano plot (Figure S1C) and confirmed that glycolytic metabolites were predominantly affected, with an accumulation of glycolytic intermediates upstream of GAPDH occurring in a dose-dependent manner (Figure S1D). To analyze the consequences of glucose metabolism imbalance, we considered a kinetic flux profiling experiment (STAR Methods) using uniformly labeled (U-^{13}C)-glucose in HCT116 cells treated at the IC_{50} over 4 hr. As expected, a reduction of ^{13}C-lactate in KA-treated cells was observed, indicating decreased flux through the glycolytic

pathway (Figure S1E). Relative levels of pentose phosphate pathway (PPP) metabolites increased in the presence of KA and flux was disrupted (Figures S1F and S1G), as was flux into glycerol metabolism (Figure S1H). In addition, KA also reduces fluxes in pathways branching from glycolysis downstream of the GAPDH step, including de novo serine (Figure S1I), entry into the tricarboxylic acid cycle (Figure S1J), and palmitate, the product of de novo lipogenesis (Figure S1K). Dose-dependent changes in energy status (Figures S1L–S1N) and redox status (Figures S1O–S1T), both essential functions of glucose metabolism, were also affected. Together, these findings indicate that KA induces global alterations in the metabolic network most consistent with direct targeting of GAPDH, with a reduction in glycolytic rate and cytotoxicity likely due to the simultaneous effects on numerous metabolic pathways and functions.

Expression of a Fungal-Derived, KA-Resistant *GAPDH* Allele Renders Human Cells Completely Resistant to KA and Reverses Their Metabolic Profile

Notably, the cytotoxic effects of targeting metabolism can often be rescued by supplementation of nutrients that restore the defective metabolic functions, as is the case of metformin and mitochondrial metabolism (Liu et al., 2016). We thus attempted to restore cell viability by modulating nutrient availability, but were unable to rescue cytotoxicity induced by KA (Figures S2A–S2E). To determine whether other mechanisms and thus possible off-target effects may account for KA cytotoxicity, we considered alternative approaches to determine whether GAPDH is the mechanistic target of KA. Notably, KA is a natural product obtained from the *Trichoderma* fungus, which thrives in anaerobic environments rich in sugar. When encountering microbes that compete for its carbon source, it secretes KA as an antibiotic to eliminate these organisms (Sakai et al., 1990; Watanabe et al., 1993), while expressing a resistant allele of *GAPDH* (*T. koningii* KAr-GAPDH) (Figure 3A). Thus, we cloned the *T. koningii* KAr-GAPDH and expressed it in human HEK293T and HCT116 cells. After verifying that human cells can express *T. koningii* KAr-GAPDH (Figures 3B and S2F), we observed that HEK293T cells expressing *T. koningii* KAr-GAPDH exhibited complete cell viability (Figure 3C) and HCT116 cells expressing *T. koningii* KAr-GAPDH exhibited almost complete viability (Figure S2G) after treatment with 0–200 μM KA. These results further demonstrated the specificity of KA toward GAPDH. In addition, while *T. koningii* KAr-GAPDH displays similarity to the active site of GAPDH with conservation of the reactive cysteine, it exhibits evolutionary divergence (Figures S2H–S2J) from mammalian GAPDH, suggesting that acquiring resistance by mutating individual GAPDH residues is difficult.

Since expression of *T. koningii* KAr-GAPDH successfully rescued cell viability in human cells treated with KA, we considered whether changes in metabolism observed in human cells treated with KA can be reversed upon KAr-GAPDH expression. After KA treatment, marked differences in metabolism in empty vector (EV)-expressing cells were observed that were completely absent in *T. koningii* KAr-GAPDH-expressing cells (Figures 3D, S2K, and S2L) and manifested in differential changes in the levels of glycolytic intermediates (Figures 3E and S2M), PPP (Figure 3F), and the TCA cycle (Figures 3G and S2N). Together, these data confirm that the mechanistic target

of KA is indeed GAPDH in part by establishing that all disruptions to metabolism are ablated when cells are engineered to be resistant to KA by expressing a resistant allele of *GAPDH*.

The Cytotoxic Response to KA Treatment Is Heterogeneous

We next measured the response to KA across a collection of 60 cancer cell lines from diverse tissue and genetic origins. At 10 μM, there was a broad, but heterogeneous, response to KA (Figure 4A) consistent with measured values of the IC_{50} for each line (Figure S3A). Consistent with earlier findings, HCT116 cells were only moderately sensitive to KA, therefore requiring a higher concentration of KA to trigger a disruption in the metabolic network. We identified three of the most resistant cell lines to KA as MCF-7, UACC-257, and NCI-H226 and their corresponding sensitive cell lines to KA as BT-549, SK-MEL-28, and NCI-H522 based on matching tissue type and subjected them to further analysis. Analysis of the cell lines considered showed that no single tissue type was more sensitive or resistant to KA (Figures S3B–S3D). We assessed whether inhibition of GAPDH activity accounts for the variability in cell line responses and found that GAPDH activity in response to KA treatment revealed little differences in the change in enzyme activity across both sensitive and resistant cells given KA at the same dose (Figures 4B and 4C). Thus, resistance to KA does not occur due to the inability to effectively inhibit GAPDH; rather, it appears to occur by another mode of action.

To determine whether nutrient supplementation could rescue cell viability in sensitive cells, we added serine and lactate, pyruvate, lactate, or 3-phosphoglycerate (3PG) to cells upon KA treatment (Figure S3E). Consistent with the findings in HCT116 cells (Figure S2E), nutrient supplementation was unable to rescue cell cytotoxicity. To determine whether differences in how KA affects metabolism contribute to the response, we generated metabolite profiles and found that sensitive cell lines revealed signatures nearly identical to those observed in previously characterized cell lines (Figures 2 and 3), whereas resistant cell lines did not show any significant metabolite alterations (Figures 4D–4F), as was also observed with kinetic flux profiling (Figures 4G, 4H, and S3F–S3H). Consistently, an accumulation of upper glycolytic intermediates and altered flux was observed only in sensitive cells (Figures 4I and S3I). Branching pathways were also affected whereby glucose flux decreased through TCA cycle intermediates and serine in a representative sensitive cell line (Figures S3J–S3M). Not surprisingly, overall TCA cycle metabolite levels remained unchanged, likely attributed to non-glucose carbon sources fueling the TCA cycle (Figure S3N). The metabolic changes observed in sensitive cells were confirmed using a pathway analysis and hierarchal clustering (Figures S4A–S4D). All together, these data strongly suggest that the heterogeneous response to KA observed across 60 cell lines can be attributed to the specific control that GAPDH exerts over the glycolytic pathway in certain cells, independent of the extent of enzyme inhibition and tissue type.

A Multi-omics Analysis Reveals that Only the Extent of the WE Predicts KA Response

We next sought to determine if any molecular features predict KA sensitivity or response. We correlated KA IC_{50} values with
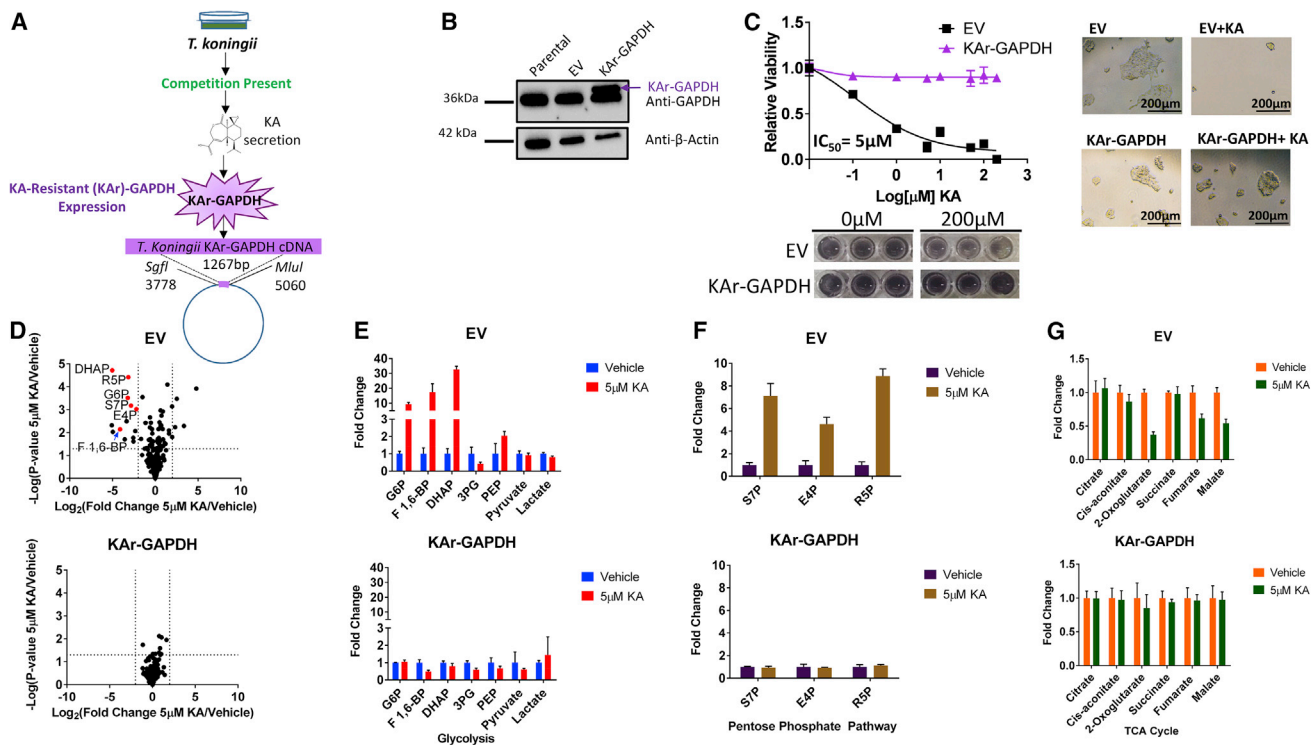
Figure 3. Expression of a Fungal-Derived, KA-Resistant *GAPDH* Allele Renders Human Cells Completely Resistant to KA and Reverses Their Metabolic Profile

(A) Schematic showing expression of a resistant allele of *GAPDH* by *Trichoderma virens*.

(B) Immunoblotting of parental, EV-, or KAr-GAPDH-expressing HEK293T cells.

(C) Cell viability of HEK293T cells expressing KAr-GAPDH or EV (top left). Representative images of well (bottom left, top right) KAr-GAPDH or EV-expressing cells treated with vehicle (0 μM) or KA (200 μM).

(D) Volcano plots showing metabolite profiles of HEK293T cells expressing EV compared to those expressing KAr-GAPDH after treatment with DMSO or 5 μM KA. Log$_2$ fold change versus $-\log_{10}$ (p value). Dotted lines along x axis represent $\pm \log_2(2)$ fold change and dotted line along y axis represents $-\log_{10}(0.05)$. Glycolysis metabolites shown as red points. All other metabolites are black points.

(E) Glycolytic metabolite levels.

(F) Pentose phosphate pathway levels.

(G) TCA cycle metabolite levels.

G6P, glucose-6-phoshate; F 1,6-BP, fructose 1,6-bisphosphate; DHAP, dihydroxyacetone phosphate; 3PG, 3-phosphoglycerate; PEP, phosphoenolpyruvate; S7P, sedoheptulose-7-phosphate; E4P, erythrose-4-phosphate; R5P, ribose-5-phosphate.

All data are represented as mean ± SEM from n = 3 biological replicates unless otherwise noted.

multiple layers of physical and molecular information including cell size, doubling time, genetic status, mRNA expression, protein expression, and metabolic uptake and excretion rates that are available in 59 of the 60 cell lines (Dolfi et al., 2013; Jain et al., 2012) (Figure 5A). Neither cell size nor doubling time correlated with response to KA (Figures 5B and 5C), nor did mutational status of several commonly mutated oncogenes and tumor suppressor genes, including *KRAS*, *PIK3CA*, *MYC*, and *TP53* (Figure S5A). Neither gene set enrichment analysis (GSEA) nor glycolytic enzyme expression reveal any significant association of any known gene sets to KA response (Figures 5D, 5E, and S5B), as was also observed when analyzing relationships with protein expression (Figures 5F and 5G). Strikingly, a comparison of metabolic uptake and excretion rates (Figure 5H) showed that glucose uptake (Spearman correlation, r = 0.60, p = 9.4 × 10^{-7}) (Figure 5I) and lactate excretion (Spearman correlation, r = 0.60, p = 5.6 × 10^{-7}) (Figure 5J), two parameters that quantitatively define the WE, had the highest Spearman correlation

coefficients and were predictive of KA response. Moreover, we found that metabolic fluxes are significantly more correlated to KA IC$_{50}$ values than to the random distribution (Figure 5K), which is not the case for mRNA and protein, which appear random (Figures 5D and 5F). Therefore, of the roughly 50,000 molecular and physical variables surveyed, only glucose uptake and lactate excretion (i.e., the WE) were predictive of KA response, allowing us to conclude that KA, and thus partial inhibition of GAPDH, specifically targets the WE.

To address the diagnostic performance of glucose uptake and lactate secretion flux as predictive measurements of KA sensitivity, we generated receiver-operating characteristic (ROC) curves and calculated the area under the curve (AUC) (Figure 5L). Notably, we found that both glucose and lactate flux are strong predictors of KA response with an AUC = 0.81, with prediction accuracy comparable to six representative targeted cancer therapies with known biomarkers. These data strongly support the clinical applicability and feasibility of using glycolytic flux, which
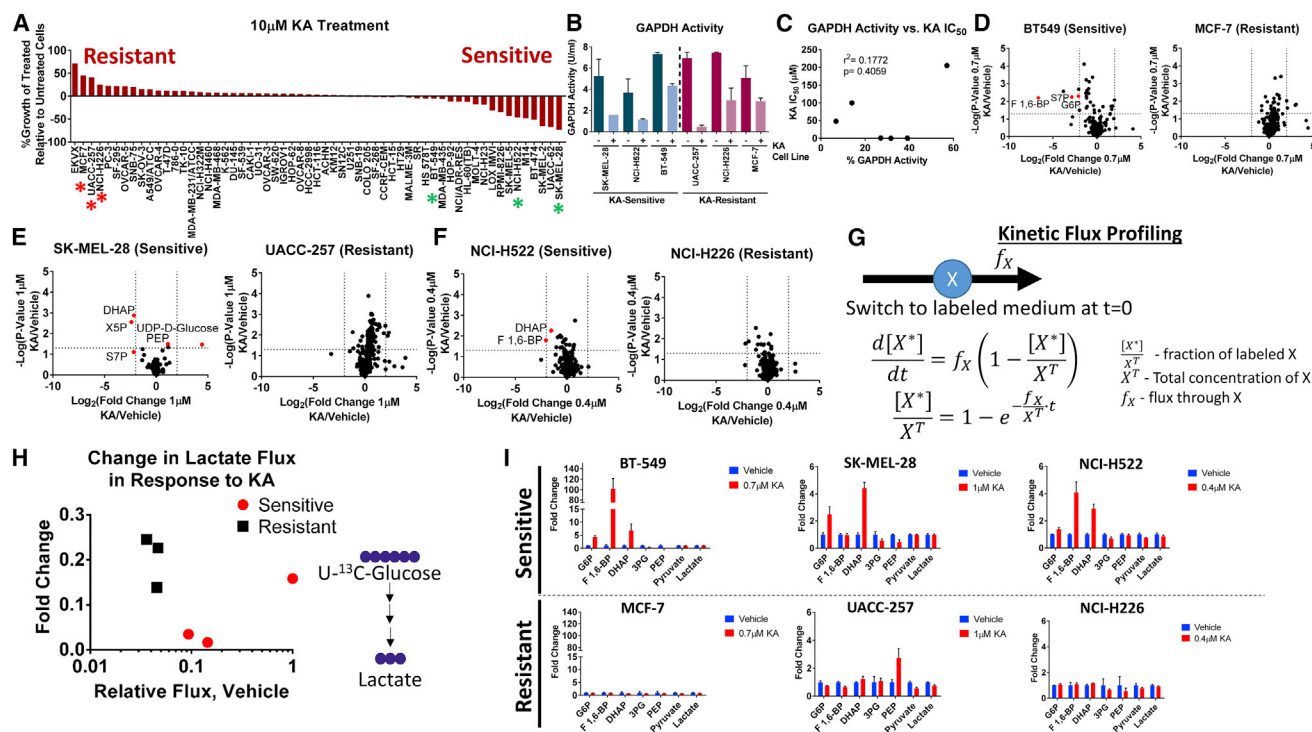
**Figure 4. The Cytotoxic Response to KA Treatment Is Heterogeneous**

(A) Waterfall plot showing the difference in response of KA to 60 independent cell lines treated with vehicle (0.01% DMSO) or 10 μM KA. Representative KA-resistant cell lines (red, *) and KA-sensitive cell lines (green, *).

(B) Relative GAPDH activity in representative KA-sensitive and KA-resistant cell lines in response to vehicle (DMSO) or KA. SK-MEL-28 and UACC-257 were treated with vehicle or 1 μM KA; NCI-H522 and NCI-H226 were treated with vehicle or 0.4 μM KA; BT-549 and MCF-7 were treated with vehicle or 0.7 μM KA (n = 2).

(C) Pearson correlation of KA IC_{50} values for KA-sensitive and KA-resistant cell lines versus percent of GAPDH activity.

(D) Volcano plots showing metabolite profiles of breast cancer cell lines after treatment with DMSO or 90 μM KA. Log_2 fold change versus $-log_{10}$ (p value). Dotted lines along x axis represent ± $log_2(2)$ fold change and dotted line along y axis represents $-log_{10}(0.05)$. Glycolysis metabolites shown as red points. All other metabolites are black points.

(E) Melanoma cell lines as in (D).

(F) Non-small-cell lung cancer cell lines as in (D).

(G) Kinetic flux profiling for lactate labeling from ^{13}C-glucose.

(H) Change in lactate flux in response to KA based on fold changes versus relative fluxes of the vehicle group from ^{13}C-lactate enrichment from U-^{13}C-glucose.

(I) Glycolysis profiles for KA-sensitive and KA-resistant breast, melanoma, and NSCLC cell lines treated with vehicle or their respective KA IC_{50} concentrations. S7P, sedoheptulose-7-phosphate; F 1,6-BP, fructose 1,6-bisphosphate; G6P, glyceraldehyde-6-phosphate; DHAP, dihydroxyacetone phosphate; X5P, xylulose-5-phosphate; PEP, phosphoenolpyruvate; UDP-D-glucose, uridine diphosphate-D-glucose.

All data are represented as mean ± SEM from n = 3 biological replicates unless otherwise noted.

---

is readily measured clinically with imaging, as a predictor of KA efficacy.

KA Is Bioavailable and Induces Dynamic Changes to Glycolysis In Vivo

Thus far, we have established that in culture, the WE can be selectively targeted by exploiting MCA and flux control through GAPDH. However, the effects on normal cells and whether a therapeutic window can be achieved in vivo are unclear. To begin to address these remaining questions, we first evaluated the effects of GAPDH inhibition in CD8+ cells since these cells are important in immune therapy settings. We found that KA does not have significant effects on proliferation, viability, or activation markers in activated CD8+ cells at lower concentrations (Figures S6A–S6I). We next evaluated the sensitivity of the highly glycolytic (Timmerman et al., 2013) estrogen-responsive breast cancer cell line BT-474 to KA (IC_{50} = 1 μM) (Figure S6J). At KA concentra-

tions corresponding to the IC_{50}, GAPDH activity was reduced and glycolysis was altered (Figures S6K–S6M). Next, ovariectomized *nu/nu* mice were implanted subcutaneously with a slow-releasing 17β-estradiol pellet and BT-474 cells were injected orthotopically into the mammary fat pad (STAR Methods). Tumors were established prior to toxicology studies (Figure 6A). One mg/kg KA was determined to be the maximum tolerated dose (MTD) based upon behavioral monitoring and adverse events at higher doses (hemolysis, hematuria, and anemia) (Figure 6B). To determine whether KA induces changes in glycolysis, we sacrificed mice over a time course of up to 24 hr and used metabolite profiling to examine the levels of glycolytic intermediates in upper glycolysis at different endpoints. Strikingly, fructose 1,6-bisphosphate (F1,6-BP) accumulated in tumors between 8 and 16 hr of treatment with 1 mg/kg KA, as did dihydroxyacetone phosphate (DHAP), albeit to a lesser extent (Figure 6C). Relative levels of 3-phosphoglycerate (3PG) and phosphoenolpyruvate (PEP)

CellPress
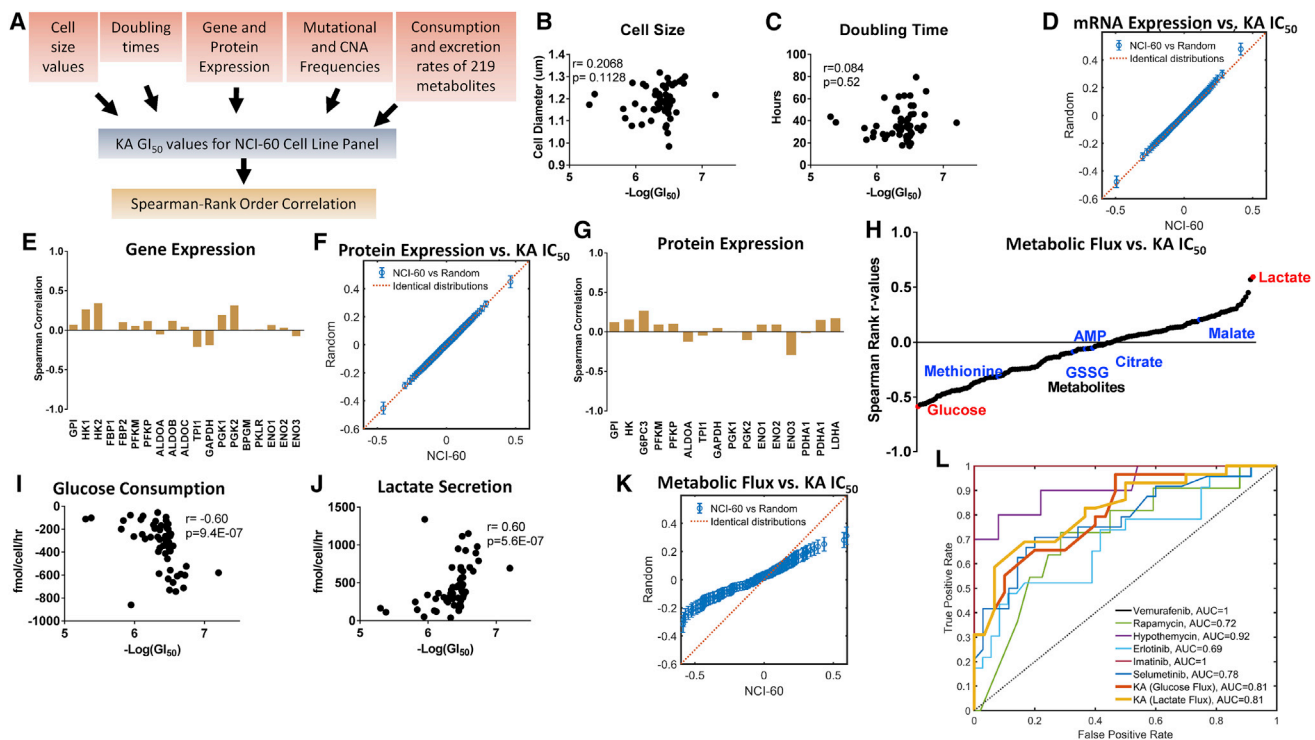
Figure 5. A Multi-omics Analysis Reveals that Only the Extent of the WE Predicts KA Response

(A) Schematic workflow of Spearman rank correlation calculations from metabolite consumption and excretion rates, cell size, doubling time, mutation, and copy number alteration (CNA) frequencies, and gene and protein expression patterns with KA IC_{50} response across NCI-60 cell line collection.

(B) Cell size correlation with KA IC_{50} response across NCI-60 cell line panel.

(C) Doubling time correlation as in (B).

(D) Quantile-quantile (Q-Q) plot comparing the quantiles from the correlation between mRNA expression levels and KA IC_{50} values in NCI-60 cell line screen with random values.

(E) Glycolysis gene expression correlation as in (B).

(F) Q-Q plot for protein expression levels as in (D).

(G) Glycolysis protein expression correlation as in (B).

(H) Correlations of uptake and secretion rates of metabolites.

(I) Glucose uptake correlation as in (B).

(J) Lactate secretion correlation as in (B).

(K) Q-Q plot for metabolic flux as in (D).

(L) Receiver-operating characteristic (ROC) curves of standard cancer therapies with specific targets and/or biomarkers. Area under the curve (AUC) assesses biomarker accuracy.

showed a decrease after 5–10 min of KA treatment, and recovered thereafter (Figure 6D). After 16 hr, upper glycolytic and PPP metabolites had the largest fold change increase (Figure 6E). At 10 min, PEP was significantly lower compared to all other detected metabolites, while 3PG had a similar trend (Figure 6F). These results indicate a dynamic effect on glycolysis whereby upper glycolytic metabolites accumulate within hours of KA treatment and lower glycolytic intermediates deplete within minutes, but then recover, likely due to a contribution of non-glucose carbon sources (Figure 6G). These data confirm that KA is bioavailable, is tolerable at certain doses, and induces acute and dynamic changes in the glycolytic network in tumors.

A Therapeutic Window for Precise Targeting of the WE with KA Can Be Achieved In Vivo

Given the bioavailability and tolerability of KA, we identified a resistant cell line to KA, MDA-MB-231 (Figures S6N and S6O), and car-

ried out metabolite profiling in the presence of KA, in which no metabolic changes were observed in response to KA treatment (Figures S6P and S6Q). We next established two orthotopic breast cancer models in which mice were injected with either sensitive BT-474 cells or resistant MDA-MB-231 cells into the mammary fat pad and were treated daily with 1 mg/kg KA, monitoring body weight and tumor growth for 14 days (Figure 7A). We determined that the circulating plasma concentration was 0.7 μM KA (Figures S7A–S7C). No significant changes in body weight were observed in BT-474 tumor-bearing mice (p = 0.37, two-tailed Student's t test) or MDA-MB-231 tumor-bearing mice (p = 0.86, two-tailed Student's t test), indicative of drug tolerability (Figure S7D). Importantly, tumor growth in KA-treated BT-474 tumor-bearing mice was substantially suppressed (p < 0.0001, two-way ANOVA), whereas tumor growth in KA-treated MDA-MB-231 cells was only marginally suppressed (p = 0.02, two-way ANOVA) over the course of 2 weeks (Figures 7B–7D). In addition, tumor morphology
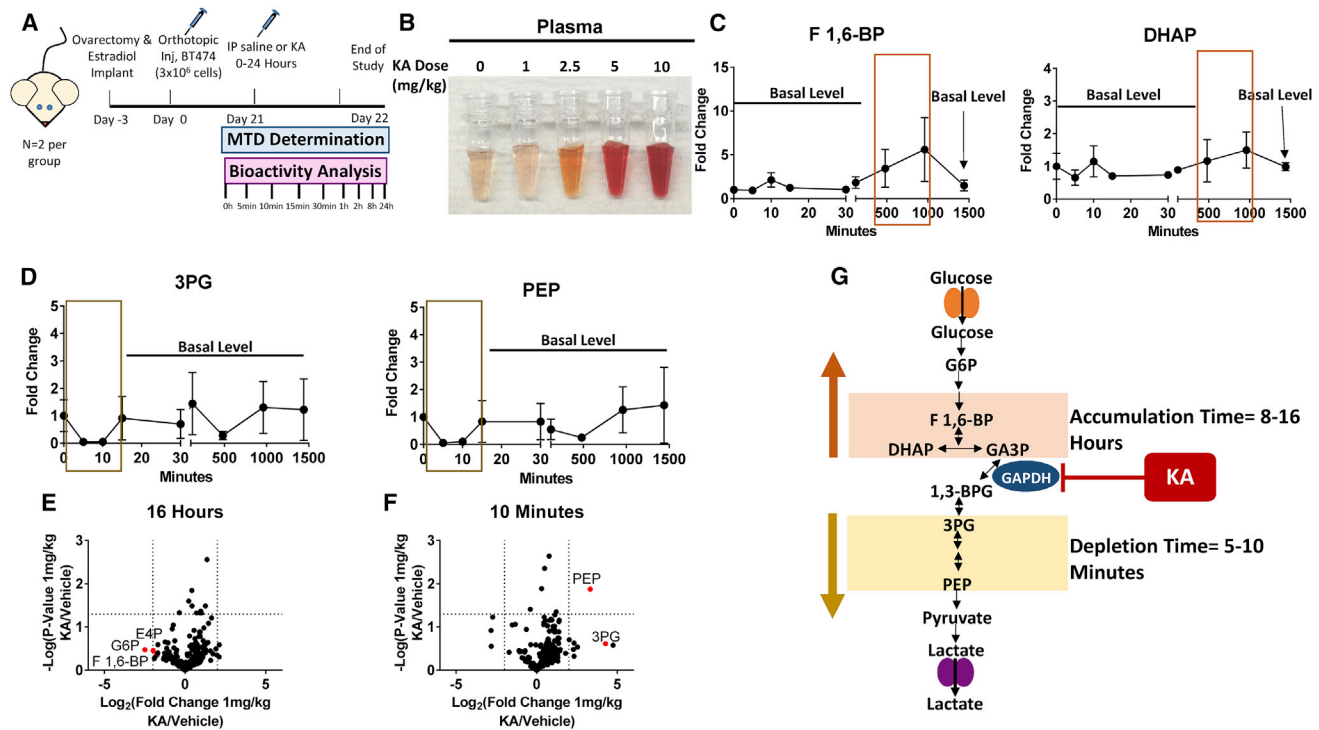
Figure 6. KA Is Bioavailable and Induces Dynamic Changes in Glycolysis In Vivo

(A) Schematic of timeline and treatment regimen of E2-treated female *nu/nu* mice injected with BT-474 cells orthotopically. These mice were treated with either saline or 1, 2.5, 5, or 10 mg/kg to identify the maximum tolerated dose (MTD) for 24 hr.

(B) Plasma from MTD analysis for doses of 0–10 mg/kg KA.

(C) Levels of upper glycolytic intermediates from 0 to 24 hr (n = 2 per group).

(D) Levels of lower glycolytic intermediates as in (C).

(E) Volcano plot showing metabolic profile at 16 hr time point. Log_2 fold change versus $-log_{10}$ (p value). Dotted lines along x axis represent $\pm log_2(2)$ fold change and dotted line along y axis represents $-log_{10}(0.05)$. Glycolysis and related metabolites shown as red points. All other metabolites are black points (n = 2).

(F) Ten minute time point as in (E).

(G) Schematic showing the dynamic response KA treatment.

G6P, glucose-6-phosphate; F 1,6-BP, fructose 1,6-bisphosphate; DHAP, dihydroxyacetone phosphate; GA3P, glyceraldehyde-3-phosphate; 1,3-BPG, 1,3-bisphosphoglycerate; 3PG, 3-phosphoglycerate; PEP, phosphoenolpyruvate.

All data are represented as mean ± SEM from biological replicates.

was markedly different in KA-treated mice and cell proliferation was significantly decreased (p = 4.0×10^{-5}, unpaired multiple t test) (Figures 7E and S7E). GAPDH is suspected to have nuclear functions in cells (Barber et al., 2005; Jung et al., 2014), but remained localized to the cytoplasm, indicative of its role in glycolysis as its primary mode of action for tumor suppression upon KA treatment (Figure 7E).

Given the efficacy of KA and issues of toxicity that typically limit further clinical evaluation of glycolysis inhibitors (Raez et al., 2013), we examined the effects on metabolism in healthy tissue. Metabolomics in skeletal muscle showed no differences upon KA treatment (Figures 7F and S7F). Metabolomics on whole blood showed as expected, altered glycolysis (Figure S7G), but no substantial differences in complete blood count (CBC) in BT-474 tumor-bearing mice (p = 0.08, two-tailed Student's t test) or in MDA-MB-231 tumor-bearing mice (p = 0.41, two-tailed Student's t test) (Figures 7G and S7H). Creatinine (p = 0.35, two-tailed Student's t test) (Figure 7H), bilirubin (p = 0.34, two-tailed Student's t test) (Figure 7I), and alanine aminotransferase (ALT) activity (p = 0.95, two-way ANOVA) (Figure 7J), markers of renal and hepatic toxicity, showed

no differences. Energy charges (ATP/ADP) in BT-474 tumor, skeletal muscle, blood, and liver also showed no significant changes (Figures S7I–S7L). Similarly, oxidized-to-reduced glutathione ratios were not altered (Figure S7M). While no changes were observed in energy metabolites in tumors, it is possible that non-glucose courses are compensating for glycolysis inhibition at longer times given changes in energy metabolites in cell culture (Figures S1L–S1T). Lastly, we determined the levels of pyruvate and lactate from multiple tissues as a readout of gluconeogenesis. We found that in KA-treated BT-474 tumor-bearing mice, pyruvate and lactate were elevated in tumors (Figure S7N), but remained mostly unchanged in liver, plasma, and muscle (Figures S7O–S7Q). These data show that KA exerts bioactivity mainly in the tumors, while sparing normal tissues.

DISCUSSION

Targeting the WE by Affecting GAPDH

There have been numerous efforts to target what have been considered to be rate-limiting steps in glycolysis (Galluzzi
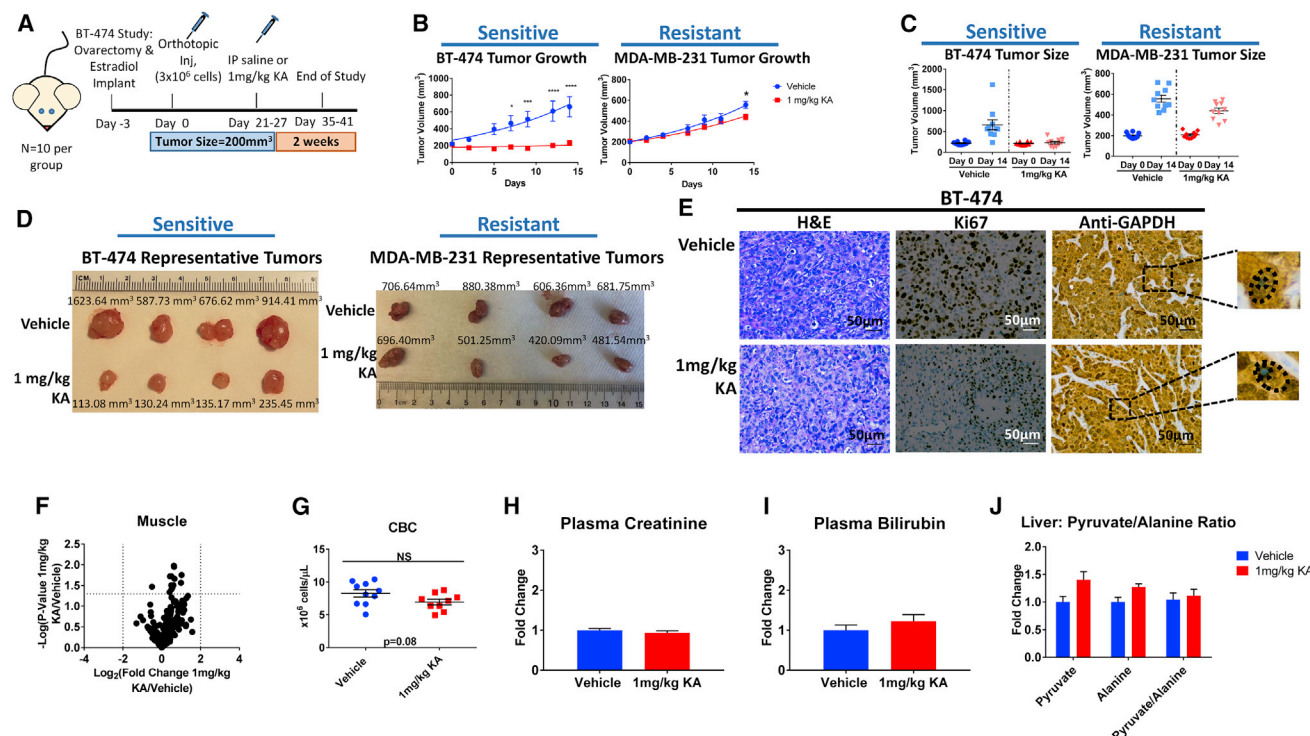
Figure 7. A Therapeutic Window for Precise Targeting of the WE with KA Can Be Achieved In Vivo

(A) Schematic of timeline and treatment of E2-treated female *nu/nu* mice injected with KA-sensitive BT-474 cells and female *nu/nu* mice injected with KA-resistant MDA-MB-231 cells orthotopically and treated with either saline or 1 mg/kg KA.

(B) Average tumor volume (mm^3) over 14 days in mice injected with BT-474 or MDA-MB-231 cells treated with vehicle or 1 mg/kg KA (n = 10 per group).

(C) Tumor volume of each individual mouse from day 0 and day 14 in the BT-474 and MDA-MB-231 tumor models (n = 10).

(D) Representative BT-474 and MDA-MB-231 tumors from vehicle-treated and 1 mg/kg KA-treated E2-treated female *nu/nu* mice on day 14.

(E) Representative hematoxylin and eosin (H&E) and immunohistochemical (IHC) staining of serial sections from *nu/nu* mice injected with BT-474 cells treated with vehicle or 1 mg/kg KA.

(F) Volcano plot showing metabolic profile from skeletal muscle treated with vehicle or 1 mg/kg KA from BT-474 tumor model. Log$_2$ fold change versus –log$_{10}$ (p value). Dotted lines along x axis represent $\pm$ log$_2$(2) fold change and dotted line along y axis represents –log$_{10}$(0.05). Significantly different metabolites shown as red points. All other metabolites are black points (n = 3).

(G) Complete blood count (CBC) for BT-474 mice treated with vehicle or 1 mg/kg KA after 14 days (n = 9 for vehicle group; n = 10 for treatment group).

(H) Relative levels of creatinine from plasma (n = 10 per group).

(I) Relative levels of bilirubin from plasma (n = 10 per group).

(J) Pyruvate, alanine, and pyruvate to alanine ratio in liver (n = 10 per group).

Data are represented as mean $\pm$ SEM, biological replicates.

*p < 0.05, **p < 0.01, ***p < 0.001, ****p < 0.0001 as determined by two-way ANOVA.

et al., 2013; Hay, 2016; Vander Heiden, 2013). Most notably, PKM2, an isoform of pyruvate kinase, has been proposed to be limiting for the WE and has been the focus of many drug development efforts. However, targeting it successfully has been challenging with numerous conflicting findings (Israelsen et al., 2013). Our results suggest that GAPDH appears to be the step in glycolysis whose regulatory properties are most different during the WE. We were able to demonstrate a remarkable selectivity toward the WE by targeting GAPDH with KA, as was concluded by evaluating the determinants of its efficacy in over 60 cell lines and in vivo. Notably, this selectivity to KA treatment was manifested across the diverse cell and tissue types of an entire mammal. Importantly, despite glycolysis being required for nearly every cell in the animal, little to no whole-body metabolic changes were observed at efficacious doses. Thus, partial inhibition of GAPDH while exhibiting selective toxicity in tumors could be tolerated in most healthy cells.

We also determined that this compound, KA, is a candidate for further pre-clinical analysis since its cytotoxicity appears to occur specifically by acting on GAPDH. We found that when KA is effective, it exerts numerous simultaneous metabolic disturbances across many pathways that are each individually considered to be targets in cancer (Locasale, 2013; Svensson et al., 2016; Weinberg and Chandel, 2015), which may be attractive for therapy.

A Natural Product with the WE as the Mechanistic Target

Other successful cancer therapeutics such as rapamycin have been isolated originally as natural products for their antibiotic activity (Vézina et al., 1975). Rapamycin was later shown to have rich underlying biology after identifying its mechanistic target, TOR. Our study provides another example of a natural product with antibiotic activity and rich underlying mammalian biology (Liberti and Locasale, 2016) as its mechanistic target (i.e., the

CellPress

WE). It is likely that in addition to being an agent with possible therapeutic value, KA will serve as a probe to more specifically explore the WE and delineate its physiological and pathophysiological functions.

MCA and Principles for Targeting Cancer Metabolism

Our findings illustrate how specific control of metabolic flux by an enzyme in a defined metabolic state can be exploited for selective targeting of that metabolic status. While MCA is widely used in broad applications such as the metabolic engineering of biofuels or antibiotic production in microbes (Bowden, 1999), our studies show that these concepts can be more broadly applicable to address biomedical questions. It should be noted that there are caveats to using MCA in that it depends on the selection and analysis of parameters and the boundary of the specific metabolic network model, and other assumptions. In addition, the assumption that the metabolic system is in steady state only partially resembles a real system. Nonetheless, we were able to show that MCA could reveal network properties of glucose metabolism specific to the WE. Importantly, we were able to use MCA to define pharmacological interventions that specifically disrupt metabolic pathways important in neoplastic settings, but render healthy tissue largely unaffected. This concept was developed by first demonstrating that during the WE, a hallmark of cancer metabolism, the rate-controlling steps in glycolysis are different than in fully oxidative energy metabolism. In this case, the effect of a change in GAPDH activity is amplified under WE conditions, as reflected by the drastic changes in glycolytic flux in KA-sensitive cells, but not KA-resistant cells (despite similar degrees of GAPDH inhibition). This differential notably is a systems-level property of how the metabolic network is configured and is independent of the specific behavior of any particular enzyme outside of the context of how the flux through the metabolic network is configured.

Comparative Metabolomics to Define Signatures of Drug Response

Altogether this study consists of a wealth of metabolomics data, with over 500 metabolite profiles generated throughout the course of this study. Although many of these compounds are commonly used as GAPDH inhibitors in the literature, we found that their metabolome-wide responses were markedly different. Using a global metabolite profile as a handle on cellular physiology, these differences in responses could be assessed and used for subsequent molecular characterization, as when we expressed a resistant allele of *GAPDH* from *Trichoderma virens* in human cells. Given the advent of this technology, we are hopeful that this resource and framework will allow for similar in-depth characterization when evaluating other pharmacological or genetic perturbations to metabolism. Such resources comparable in scope have been documented for yeast, as in a recent study that evaluated the amino acid profiles of a yeast deletion library (Mülleder et al., 2016). This current analysis enables characterization of a phenotypic response in mammalian systems.

Metabolism and Precision Medicine

Therapeutic applications to cancer metabolism have often been limited by defining the appropriate contexts in which a given agent may be effective. Unlike cases in which genetic status determines the success or failure of a given therapy, therapies that affect metabolism may have more complicated biomarkers, if any. In fact, recent studies have suggested that environmental factors such as tissue type or nutritional status have a larger influence on cancer cell metabolism (Davidson et al., 2016; Hensley et al., 2016; Mayers et al., 2016; Yuneva et al., 2012) than the genetic lesions that have been thought to determine the extent of the WE (Vander Heiden et al., 2009). Therefore, the metabolic state of the tumor is a complex function of genetic, protein, and environmental status. Consistent with these findings, we remarkably found that of over 50,000 variables surveyed, including the mutational status of oncogenes that are known to influence the WE, only a specific configuration of metabolism involving the extent of glucose uptake and lactate secretion was predictive of the outcome of a treatment with an agent that targets a glycolytic enzyme. Thus, this study provides one of the first examples of a targeted agent whose biomarker cannot be defined by genetic status, but by the value of a specific metabolic flux. Since metabolite measurements are routinely used clinically as diagnostics and FDG-PET uptake, which is a surrogate for glycolytic rate, as a standard approach to monitor tumor progression, our findings could be straightforwardly employed in the clinic. Importantly, this study demonstrates that a complete understanding of pharmacogenomics (Iorio et al., 2016) that uses multi-omics data to predict drug responses also likely requires information encoded at the level of metabolites and metabolic fluxes.

STAR★METHODS

Detailed methods are provided in the online version of this paper and include the following:

- KEY RESOURCES TABLE
- CONTACT FOR REAGENT AND RESOURCE SHARING
- EXPERIMENTAL MODEL AND SUBJECT DETAILS
  - Cell Culture
  - CD8 Activation
  - Animal Experiments
- METHOD DETAILS
  - Drug Treatments
  - Cell Viability Assays
  - Nutrient Supplementation in Media
  - Tumor Cell Line Sensitivity Analysis
  - GAPDH Activity Assay
  - Lentiviral Transfection and Transduction
  - Immunoblotting
  - Culture and Isolation of Koningic Acid from *Trichoderma virens*
  - Isolation and Purification of Koningic Acid
  - U-^{13}C-Glucose Stable Isotope Labeling
  - Metabolite Extraction
  - Liquid Chromatography
  - Mass Spectrometry
  - Peak Extraction and Data Analysis
  - Kinetic flux profiling
  - Thermodynamic and Kinetic Analysis
  - Integrative Analysis of Drug Response and Multi-omics Data

CellPress

○ Koningic Acid Docking to GAPDH
○ GAPDH Protein Multiple Sequence Alignment Comparisons
○ Analysis of Metabolomics Data
○ Paraffin Embedding and Immunohistochemistry
● QUANTIFICATION AND STATISTICAL ANALYSIS
● DATA AND SOFTWARE AVAILABILITY

SUPPLEMENTAL INFORMATION

Supplemental Information includes seven figures and can be found with this article online at http://dx.doi.org/10.1016/j.cmet.2017.08.017.

AUTHOR CONTRIBUTIONS

Conceptualization, M.V.L. and J.W.L.; Animal Experiments, S.E.W., D.P.M., M.V.L., X.G., and R.B.; Koningic Acid Isolation and Purification, M.V.L., J.A.B., and F.C.S.; Metabolomics, M.V.L. and X.L.; Data Analysis, M.V.L., M.M., M.O.J., J.C.R., Z.D., N.S.M., O.E., and I.I.C.C.; Mathematical Modeling, Z.D. and A.A.S.; All Other Experiments, M.V.L.; Writing, M.V.L. and J.W.L.; Supervision, M.V.L. and J.W.L.

REFERENCES

Barber, R.D., Harmer, D.W., Coleman, R.A., and Clark, B.J. (2005). GAPDH as a housekeeping gene: analysis of GAPDH mRNA expression in a panel of 72 human tissues. Physiol. Genomics 21, 389–395.

Bowden, A.C. (1999). Metabolic control analysis in biotechnology and medicine. Nat. Biotechnol. 17, 641–643.

Campbell-Burk, S.L., Jones, K.A., and Shulman, R.G. (1987). 31P NMR saturation-transfer measurements in Saccharomyces cerevisiae: characterization of phosphate exchange reactions by iodoacetate and antimycin A inhibition. Biochemistry 26, 7483–7492.

Collins, F.S., and Varmus, H. (2015). A new initiative on precision medicine. N. Engl. J. Med. 372, 793–795.

Dai, J., Weinberg, R.S., Waxman, S., and Jing, Y. (1999). Malignant cells can be sensitized to undergo growth inhibition and apoptosis by arsenic trioxide through modulation of the glutathione redox system. Blood 93, 268–277.

Davidson, S.M., Papagiannakopoulos, T., Olenchock, B.A., Heyman, J.E., Keibler, M.A., Luengo, A., Bauer, M.R., Jha, A.K., O'Brien, J.P., Pierce, K.A., et al. (2016). Environment impacts the metabolic dependencies of Ras-driven non-small cell lung cancer. Cell Metab. 23, 517–528.

Dolfi, S.C., Chan, L.L.-Y., Qiu, J., Tedeschi, P.M., Bertino, J.R., Hirshfield, K.M., Oltvai, Z.N., and Vazquez, A. (2013). The metabolic demands of cancer cells are coupled to their size and protein synthesis rates. Cancer Metab. 1, 20.

Endo, A., Hasumi, K., Sakai, K., and Kanbe, T. (1985). Specific inhibition of glyceraldehyde-3-phosphate dehydrogenase by koningic acid (heptelidic acid). J. Antibiot. 38, 920–925.

Fell, D.A. (1992). Metabolic control analysis: a survey of its theoretical and experimental development. Biochem. J. 286, 313–330.

Fischer, A.H., Jacobson, K.A., Rose, J., and Zeller, R. (2008a). Paraffin embedding tissue samples for sectioning. CSH Protoc. 2008, t4989.

Fischer, A.H., Jacobson, K.A., Rose, J., and Zeller, R. (2008b). Hematoxylin and eosin staining of tissue and cell sections. CSH Protoc. 2008, t4986.

Galluzzi, L., Kepp, O., Vander Heiden, M.G., and Kroemer, G. (2013). Metabolic targets for cancer therapy. Nat. Rev. Drug Discov. 12, 829–846.

Ganapathy-Kanniappan, S., Geschwind, J.-F.H., Kunjithapatham, R., Buijs, M., Vossen, J.A., Tchernyshyov, I., Cole, R.N., Syed, L.H., Rao, P.P., Ota, S., and Vali, M. (2009). Glyceraldehyde-3-phosphate dehydrogenase (GAPDH) is pyruvylated during 3-bromopyruvate mediated cancer cell death. Anticancer Res. 29, 4909–4918.

Garber, K. (2016). Cancer anabolic metabolism inhibitors move into clinic. Nat. Biotechnol. 34, 794–795.

Gholami, A.M., Hahne, H., Wu, Z., Auer, F.J., Meng, C., Wilhelm, M., and Kuster, B. (2013). Global proteome analysis of the NCI-60 cell line panel. Cell Rep. 4, 609–620.

Grosdidier, A., Zoete, V., and Michielin, O. (2011). SwissDock, a protein-small molecule docking web service based on EADock DSS. Nucleic Acids Res. 39, W270–W277.

Hay, N. (2016). Reprogramming glucose metabolism in cancer: can it be exploited for cancer therapy? Nat. Rev. Cancer 16, 635–649.

Heinrich, R., and Schuster, S. (1996). The Regulation of Cellular Systems (Chapman & Hall).

Hensley, C.T., Faubert, B., Yuan, Q., Lev-Cohain, N., Jin, E., Kim, J., Jiang, L., Ko, B., Skelton, R., Loudat, L., et al. (2016). Metabolic heterogeneity in human lung tumors. Cell 164, 681–694.

Iorio, F., Knijnenburg, T.A., Vis, D.J., Bignell, G.R., Menden, M.P., Schubert, M., Aben, N., Gonçalves, E., Barthorpe, S., Lightfoot, H., et al. (2016). A landscape of pharmacogenomic interactions in cancer. Cell 166, 740–754.

Irwin, J.J., and Shoichet, B.K. (2005). ZINC—a free database of commercially available compounds for virtual screening. J. Chem. Inf. Model. 45, 177–182.

Irwin, J.J., Sterling, T., Mysinger, M.M., Bolstad, E.S., and Coleman, R.G. (2012). ZINC: a free tool to discover chemistry for biology. J. Chem. Inf. Model. 52, 1757–1768.

Israelsen, W.J., Dayton, T.L., Davidson, S.M., Fiske, B.P., Hosios, A.M., Bellinger, G., Li, J., Yu, Y., Sasaki, M., Horner, J.W., et al. (2013). PKM2 isoform-specific deletion reveals a differential requirement for pyruvate kinase in tumor cells. Cell 155, 397–409.

Jain, M., Nilsson, R., Sharma, S., Madhusudhan, N., Kitami, T., Souza, A.L., Kafri, R., Kirschner, M.W., Clish, C.B., and Mootha, V.K. (2012). Metabolite profiling identifies a key role for glycine in rapid cancer cell proliferation. Science 336, 1040–1044.

Jung, D.-W., Kim, W.-H., Seo, S., Oh, E., Yim, S.-H., Ha, H.-H., Chang, Y.-T., and Williams, D.R. (2014). Chemical targeting of GAPDH moonlighting function in cancer cells reveals its role in tubulin regulation. Chem. Biol. 21, 1533–1545.

Kyte, J., and Doolittle, R.F. (1982). A simple method for displaying the hydropathic character of a protein. J. Mol. Biol. 157, 105–132.

Larkin, M.A., Blackshields, G., Brown, N.P., Chenna, R., McGettigan, P.A., McWilliam, H., Valentin, F., Wallace, I.M., Wilm, A., Lopez, R., et al. (2007). Clustal W and Clustal X version 2.0. Bioinformatics 23, 2947–2948.

Lehninger, A.L., Nelson, D.L., and Cox, M.M. (2013). Lehninger Principles of Biochemistry, Sixth Edition (W.H. Freeman).

Liberti, M.V., and Locasale, J.W. (2016). The Warburg effect: how does it benefit cancer cells? Trends Biochem. Sci. 41, 211–218.

Liu, X., Ser, Z., Cluntun, A.A., Mentch, S.J., and Locasale, J.W. (2014a). A strategy for sensitive, large scale quantitative metabolomics. J. Vis. Exp. 51358.

Liu, X., Ser, Z., and Locasale, J.W. (2014b). Development and quantitative evaluation of a high-resolution metabolomics technology. Anal. Chem. 86, 2175–2184.

Liu, X., Romero, I.L., Litchfield, L.M., Lengyel, E., and Locasale, J.W. (2016). Metformin targets central carbon metabolism and reveals mitochondrial requirements in human cancers. Cell Metab. 24, 728–739.

Locasale, J.W. (2013). Serine, glycine and one-carbon units: cancer metabolism in full circle. Nat. Rev. Cancer 13, 572–583.

Madhukar, N.S., Warmoes, M.O., and Locasale, J.W. (2015). Organization of enzyme concentration across the metabolic network in cancer cells. PLoS One 10, e0117131.

Mayers, J.R., Torrence, M.E., Danai, L.V., Papagiannakopoulos, T., Davidson, S.M., Bauer, M.R., Lau, A.N., Ji, B.W., Dixit, P.D., Hosios, A.M., et al. (2016). Tissue of origin dictates branched-chain amino acid metabolism in mutant Kras-driven cancers. Science 353, 1161–1165.

Mülleder, M., Calvani, E., Alam, M.T., Wang, R.K., Eckerstorfer, F., Zelezniak, A., and Ralser, M. (2016). Functional metabolomics describes the yeast biosynthetic regulome. Cell 167, 553–565.e12.

Németi, B., and Gregus, Z. (2005). Reduction of arsenate to arsenite by human erythrocyte lysate and rat liver cytosol - characterization of a glutathione- and NAD-dependent arsenate reduction linked to glycolysis. Toxicol. Sci. 85, 847–858.

Noor, E., Bar-Even, A., Flamholz, A., Reznik, E., Liebermeister, W., and Milo, R. (2014). Pathway thermodynamics highlights kinetic obstacles in central metabolism. PLoS Comput. Biol. 10, e1003483.

Pettersen, E.F., Goddard, T.D., Huang, C.C., Couch, G.S., Greenblatt, D.M., Meng, E.C., and Ferrin, T.E. (2004). UCSF Chimera—a visualization system for exploratory research and analysis. J. Comput. Chem. 25, 1605–1612.

Raez, L.E., Papadopoulos, K., Ricart, A.D., Chiorean, E.G., Dipaola, R.S., Stein, M.N., Rocha Lima, C.M., Schlesselman, J.J., Tolba, K., Langmuir, V.K., et al. (2013). A phase I dose-escalation trial of 2-deoxy-D-glucose alone or combined with docetaxel in patients with advanced solid tumors. Cancer Chemother. Pharmacol. 71, 523–530.

Sakai, K., Hasumi, K., and Endo, A. (1988). Inactivation of rabbit muscle glyceraldehyde-3-phosphate dehydrogenase by koningic acid. Biochim. Biophys. Acta 952, 297–303.

Sakai, K., Hasumi, K., and Endo, A. (1990). Two glyceraldehyde-3-phosphate dehydrogenase isozymes from the koningic acid (heptelidic acid) producer Trichoderma koningii. Eur. J. Biochem. 193, 195–202.

Sakai, K., Hasumi, K., and Endo, A. (1991). Identification of koningic acid (heptelidic acid)-modified site in rabbit muscle glyceraldehyde-3-phosphate dehydrogenase. Biochim. Biophys. Acta 1077, 192–196.

Sauro, H.M., Hucka, M., Finney, A., Wellock, C., Bolouri, H., Doyle, J., and Kitano, H. (2003). Next generation simulation tools: the Systems Biology Workbench and BioSPICE integration. OMICS 7, 355–372.

Shestov, A.A., Liu, X., Ser, Z., Cluntun, A.A., Hung, Y.P., Huang, L., Kim, D., Le, A., Yellen, G., Albeck, J.G., and Locasale, J.W. (2014). Quantitative determinants of aerobic glycolysis identify flux through the enzyme GAPDH as a limiting step. Elife 3, e03342.

Shoemaker, R.H. (2006). The NCI60 human tumour cell line anticancer drug screen. Nat. Rev. Cancer 6, 813–823.

Sievers, F., Wilm, A., Dineen, D., Gibson, T.J., Karplus, K., Li, W., Lopez, R., McWilliam, H., Remmert, M., Söding, J., et al. (2011). Fast, scalable generation of high-quality protein multiple sequence alignments using Clustal Omega. Mol. Syst. Biol. 7, 539.

Svensson, R.U., Parker, S.J., Eichner, L.J., Kolar, M.J., Wallace, M., Brun, S.N., Lombardo, P.S., Van Nostrand, J.L., Hutchins, A., Vera, L., et al. (2016). Inhibition of acetyl-CoA carboxylase suppresses fatty acid synthesis and tumor growth of non-small-cell lung cancer in preclinical models. Nat. Med. 22, 1108–1119.

Timmerman, L.A., Holton, T., Yuneva, M., Louie, R.J., Padró, M., Daemen, A., Hu, M., Chan, D.A., Ethier, S.P., van 't Veer, L.J., et al. (2013). Glutamine sensitivity analysis identifies the xCT antiporter as a common triple-negative breast tumor therapeutic target. Cancer Cell 24, 450–465.

Vander Heiden, M.G. (2013). Exploiting tumor metabolism: challenges for clinical translation. J. Clin. Invest. 123, 3648–3651.

Vander Heiden, M.G., and DeBerardinis, R.J. (2017). Understanding the intersections between metabolism and cancer biology. Cell 168, 657–669.

Vander Heiden, M.G., Cantley, L.C., and Thompson, C.B. (2009). Understanding the Warburg effect: the metabolic requirements of cell proliferation. Science 324, 1029–1033.

Vézina, C., Kudelski, A., and Sehgal, S.N. (1975). Rapamycin (AY-22,989), a new antifungal antibiotic. I. Taxonomy of the producing streptomycete and isolation of the active principle. J. Antibiot. 28, 721–726.

Watanabe, H., Hasumi, K., Fukushima, Y., Sakai, K., and Endo, A. (1993). Cloning of two isozymes of Trichoderma koningii glyceraldehyde-3-phosphate dehydrogenase with different sensitivity to koningic acid. Biochim. Biophys. Acta 1172, 43–48.

Weinberg, S.E., and Chandel, N.S. (2015). Targeting mitochondria metabolism for cancer therapy. Nat. Chem. Biol. 11, 9–15.

Xia, J., Sinelnikov, I.V., Han, B., and Wishart, D.S. (2015). MetaboAnalyst 3.0—making metabolomics more meaningful. Nucleic Acids Res. 43 (W1), W251–W257.

Yuneva, M.O., Fan, T.W., Allen, T.D., Higashi, R.M., Ferraris, D.V., Tsukamoto, T., Matés, J.M., Alonso, F.J., Wang, C., Seo, Y., et al. (2012). The metabolic profile of tumors depends on both the responsible genetic lesion and tissue type. Cell Metab. 15, 157–170.

CellPress

STAR★METHODS

KEY RESOURCES TABLE

REAGENT or RESOURCE	SOURCE	IDENTIFIER
Antibodies		
Rabbit Polyclonal Anti-GAPDH	Abcam	Cat# ab9485; RRID: AB_307275
Mouse Monoclonal Anti-β-Actin	Thermo Scientific	Cat# MA5-15739; RRID: AB_10979409
Mouse IgG (H&L) Antibody Peroxidase Conjugated	Rockland	Cat# 610-1302; RRID: AB_219656
Rabbit IgG (H&L) Antibody Peroxidase Conjugated	Rockland	Cat# 611-7302; RRID: AB_219747
CD3e Monoclonal Antibody	eBioscience	Cat# 16-0031-85; RRID: AB_468848
CD28 Monoclonal Antibody	eBioscience	Cat# 16-0281-85; RRID: AB_468922
CD8a Monoclonal Antibody, APC	eBioscience	Cat # 17-0081-82; RRID: AB_469335
CD62L Monoclonal Antibody, APC	eBioscience	Cat# 17-0621-82; RRID: AB_469410
CD44 Monoclonal Antibody, PE	eBioscience	Cat# 12-0441-82; RRID: AB_465664
CD62L Monoclonal Antibody, FITC	eBioscience	Cat# 11-0621-81; RRID: AB_465108
Granzyme B Monoclonal Antibody, PE	eBioscience	Cat# 12-8898-80; RRID: AB_10853811
Biotinylated Goat Anti-Rabbit	Thermo Scientific	Cat# BA-1000
ABC Elite	Vector	Cat# PK-7100; RRID: AB_2336827
Anti-Rabbit HQ	Abcam	Cat# 760-4815
Anti-HQ System	Roche/Ventana	Cat# 760-4820
Chemicals, Peptides, and Recombinant Proteins		
Koningic Acid	This paper; Adipogen	Cat# AG-CN2-0118-M001
Arsenate	Sigma-Aldrich	Cat# A6756; CAS: 10048-95-0
Arsenic Trioxide	Sigma-Aldrich	Cat# 17971; CAS: 1327-53-3
3-Bromopyruvic Acid	Sigma-Aldrich	Cat# 16490; CAS: 1113-59-3
Sodium Iodoacetate	Sigma Aldrich	Cat# I2512; CAS: 305-53-3
N-acetyl-L-cysteine	Sigma-Aldrich	Cat# A9165; CAS: 616-91-1
Sodium Pyruvate	Santa Cruz Biotechnology	Cat# sc-208397; CAS: 113-24-6
Sodium Lactate	Santa Cruz Biotechnology	Cat# sc-253582; CAS: 72-17-3
L-Serine	Amresco	Cat# 1B1103; CAS: 56-45-1
D-(-)-3-Phosphoglyceric acid disodium salt	Sigma-Aldrich	Cat# P8877; CAS: 80731-10-8
D-Glucose (U-13C6, 99%)	Cambridge Isotope Laboratories	Cat# CLM-1396; CAS: 110187-42-3
Acetonitrile, Optima LC-MS	Fisher Scientific	Cat# A955; CAS: 75-05-8
Water, Optima LC-MS	Fisher Scientific	Cat# W6; CAS: 7732-18-5
Methanol, Optima LC-MS	Fisher Scientific	Cat# A456; CAS: 67-56-1
HPLC Grade Methanol	Fisher Scientific	Cat# A452; CAS: 67-56-1
Potato Dextrose Agar	Fisher Scientific	Cat# DF0013-17-6
Malt Extract	BD Biosciences	Cat# 218630
Glucose	VWR	Cat# 97061-168; CAS 50-99-7
Peptone	BD Biosciences	Cat#: 211677
Acetic Acid, Glacial (Certified ACS)	Fisher Scientific	Cat# A38-500; CAS: 64-19-7
Matrigel	Corning	Cat# 354234
17β-Estradiol Pellets	Innovative Research of America	Cat# SE-121
Sulfamethoxazole and Trimethoprim Oral Suspension, USP (Septra)	Hi-Tech Pharmacal Company	NDC: 50383-823-16
IL-2 Recombinant Protein	eBioscience	Cat# 14-8021-64

(Continued on next page)

CellPress

Continued

REAGENT or RESOURCE	SOURCE	IDENTIFIER
IL-7 Recombinant Protein	Peprotech	Cat# 217-17
Propidium Iodide	Sigma-Aldrich	Cat# P4864
Critical Commercial Assays		
Vybrant MTT Cell Proliferation Assay Kit	Thermo Fisher Scientific	Cat# M6494
GAPDH Activity Assay Kit	BioVision	Cat# K680
JetPRIME DNA Transfection Reagent	Polyplus Transfection	Cat# 114-07
Clarity Western ECL Detection Kit	Bio-Rad	Cat# 1705061
CD8+ T Cell Isolation Kit, Mouse	Miltenyi Biotec	Cat# 130-095-236
CellTrace Violet Cell Proliferation Kit	LifeTech	Cat# C34557
Deposited Data		
Metabolomics Data	This paper; Mendeley Data	http://dx.doi.org/10.17632/wmk2prwynj.1
Experimental Models: Cell Lines		
Human: UACC-257 cells	National Cancer Institute	N/A
Human: HEK293T cells	ATCC	CRL-3216
Human: HCT116 cells	ATCC	CCL-247
Human: BT-549 cells	ATCC	HTB-122
Human: MCF-7 cells	ATCC	HTB-22
Human: SK-MEL-28 cells	ATCC	HTB-72
Human: NCI-H522 cells	ATCC	CRL-5810
Human: NCI-H226 cells	ATCC	CRL-5826
Human: BT-474 cells	ATCC	HTB-20
Human: MDA-MB-231 cells	ATCC	HTB-26
Experimental Models: Organisms/Strains		
Mouse: $Foxn1^{nu}$	The Jackson Laboratory	007850
Mouse: C57BL/6J	The Jackson Laboratory	000664
Recombinant DNA		
cDNA: Trichoderma koningii mRNA for GAPDH, clone: pT56	Origene	GenBank: D14519.1
pLenti-C-Myc-DDK-IRES-Puro Expression Vector	Origene/Blue Heron	Cat# PS100069
PsPAX2 Plasmid	Addgene	Addgene 12260
PMD2.G Plasmid	Addgene	Addgene 12259
Software and Algorithms		
ZINC Database	Irwin and Shoichet, 2005; Irwin et al., 2012	http://zinc.docking.org; ZINC ID: ZINC 15272438
Swiss Dock Server	Grosdidier et al., 2011	http://www.swissdock.ch
UCSF Chimera 1.10.2	Pettersen et al., 2004	http://www.rbvi.ucsf.edu/chimera
Clustal Omega	Sievers et al., 2011	http://www.ebi.ac.uk/Tools/msa/clustalo/
Clustal W2-Phylogeny	Larkin et al., 2007	http://www.ebi.ac.uk/Tools/phylogeny/simple_phylogeny/
BioModels Database	EMBL-EBI	http://www.ebi.ac.uk/biomodels-main/; Model ID: MODEL1504010000
GraphPad Prism 6	GraphPad	http://www.graphpad.com/scientific-software/prism/
Sieve 2.0	Thermo Scientific	https://www.thermofisher.com/order/catalog/product/IQLAAEGABSFAHSMAPV
GENE-E/Morpheus Software	The Broad Institute	https://software.broadinstitute.org/GENE-E/index.html
MetaboAnalyst 3.0	Xia et al., 2015	http://www.metaboanalyst.ca/faces/home.xhtml
ImageJ	NIH	https://imagej.nih.gov/ij/index.html

(Continued on next page)

Continued

REAGENT or RESOURCE	SOURCE	IDENTIFIER
MATLAB	MathWorks	https://www.mathworks.com/product/matlab.html
GNU Scientific Library	Free Software Foundation	http://www.gnu.org/software/gsl/
Systems Biology Workbench	Sauro et al., 2003	http://sbw.sourceforge.net/
R-Statistical Programming	The R Foundation	https://www.r-project.org/
Gene Set Enrichment Analysis	The Broad Institute	http://software.broadinstitute.org/gsea/index.jsp
CellMiner	National Cancer Institute	https://discover.nci.nih.gov/cellminer/
FlowJo V10	Tree Star, LLC	https://www.flowjo.com/
Other		
Trichoderma virens: von Arx, anamorph: G-4 strain	ATCC	MYA-297

CONTACT FOR REAGENT AND RESOURCE SHARING

Further information and requests for reagents may be directed to and will be fulfilled by the Lead Contact, Jason W. Locasale (jason.locasale@duke.edu).

EXPERIMENTAL MODEL AND SUBJECT DETAILS

Cell Culture

All cells were cultured in full media containing RPMI-1640 (GIBCO), 10% heat-inactivated fetal bovine serum (FBS), 100U/mL penicillin, and 100mg/ml streptomycin. All cell lines were obtained from the American Tissue Culture Collection (ATCC), except UACC-57, which was obtained from the National Cancer Institute (NCI) at the National Institutes of Health (Bethesda, MD, USA). Cells were cultured in a 37°C, 5% CO_2 atmosphere. For koningic acid (KA) dose response curves, either KA (Adipogen, #AG-N2-0118-M001; Isolated In-House) solubilized in water was added to the media at the respective concentrations or 0.01% water for the vehicle. At the start of each experiment, cells were seeded at a density of $1x10^6$ cells for 10cm plates for protein collection, $3x10^5$ cells/well in a 6-well plate for metabolite collection, and $5x10^3$ cells/well in a 96-well plate for cell viability and activity assays. Cells were allowed to adhere for 24 hr.

CD8 Activation

CD8+ cells were isolated from the spleens of 8-12 week old C57BL/6J mice (The Jackson Laboratory, 000664) fed standard chow maintained under IACUC approved protocols. CD8+ cells isolated to greater than 95% purity by CD8+ negative isolation kit (Miltenyi, #130-095-236). CD8+ cells were stained using the proliferative dye Cell Trace Violet (LifeTech, #C34557) before stimulation as per manufacturer's protocol. Cells were stimulated on 5 μg/mL anti-CD3/CD28-coated plates (ebioscience, aCD3 #16-0031-85; aCD28 #16-0281-85) in RPMI 1640 media containing IL-2 ('activated', eBioscience, #14-8021-64, 10 ng/mL), or in tissue-culture treated plates in media containing IL-7 ('naive', Peprotech, #217-17), 1 ng/mL) for up to 7 days. Drug was added at the beginning of activation. Cells were removed at each day described for viability (Propidium Iodide, Sigma-Aldrich, #P4864), cell counts, proliferation, and/or surface markers of activation. Cell surface markers used were CD8-APC (ebioscience, #17-0081-82), CD62L-APC (ebioscience, #17-0621-82), CD44-PE (ebioscience, #12-0441-82), and CD62L-FITC (ebioscience, #11-0621-81). At day 4 and 7, cells were removed for intracellular granzyme B PE stain (ebioscience, #12-8898-80). All data were acquired in triplicate on a MacsQuant Analyzer (Miltenyi Biotec) and analyzed using FlowJo V10 (TreeStar software).

Animal Experiments

All animal experiments were performed in compliance with guidelines of the Animal Welfare Act and the guide for the care and use of laboratory animals following protocols approved by the Duke University Institutional Animal Care and Use Committee (IACUC) protocol number A011-16-01. For BT-474 tumor bearing mice, 6-week old female *Foxn1^nu* mice (The Jackson Laboratory, 007850) were ovariectomized and subcutaneously implanted at surgery with 0.72 mg/60 day estradiol pellets (Innovative Research of America, #SE-121). Septra antibiotic treatment (Hi-Tech Pharmacal, 50383-823-16) (drinking water) was initiated at this time and continued throughout the study. Two days later, $3x10^6$ BT-474 breast cancer cells (mixed 1:1 with Matrigel) (Corning, #354234) were injected orthotopically into the mammary fat pad. For MDA-MB-231 tumor bearing mice, 6-week old female *nu/nu* mice (internal breeding colony) were injected orthotopicallly with $3x10^6$ MDA-MB-231 breast cancer cells (mixed 1:1 with Matrigel) into the mammary fat pad. Tumor volume, animal body weight, and behavior were evaluated 3 times weekly until tumors reached $200mm^3$ volume. At that point, BT-474 tumor bearing mice were randomized to the following treatment groups for daily intraperitoneal (IP) injections to determine the maximum tolerated dose (MTD): vehicle (5% DMSO/95% sterile saline), 1 mg/kg KA, 2.5 mg/kg KA, 5 mg/kg KA, and 10 mg/kg KA. MDA-MB-231 tumor bearing mice were randomized to vehicle (5% DMSO/95% sterile saline) and 1 mg/kg KA. KA was resuspended in DMSO prior to dilution in saline immediately prior to use. Mice were evaluated during treatment daily

CellPress

for behavior and 3X weekly for weight loss. Mice receiving > 1 mg/kg KA were euthanized 24-48 hr after administration due to human endpoints (behavior, hematuria, and anemia), and 1 mg/kg KA was determined to be the MTD. Tumor measurements were taken three times weekly for 2 weeks. For efficacy studies, after 2 weeks of treatment, the mice were anesthetized with isoflurane and euthanized by cervical dislocation 30 min after the final administration of KA prior to harvest of tumors and tissues for analysis. For pharmacokinetics analysis, mice were treated with vehicle or 1 mg/kg KA from 0-24 hr, and anesthetized and euthanized at different time points by the same methods already described, followed by tumor and tissue collection. For metabolomics, tumors, tissue, and plasma were flash frozen in liquid nitrogen. For immunohistochemistry, tumors and tissue were fixed in 10% formalin. For complete blood count (CBC) analysis, whole blood was mixed with 0.9% sodium chloride (1:200) and cells were counted using a hemocytometer.

METHOD DETAILS

Drug Treatments
For all cell lines, IC_{50} values were measured by seeding 5×10^3 cells/well in triplicate in a 96-well plate and allowed to adhere for 24 hr. The following day, 0-500 μM concentrations of either vehicle (DMSO), arsenate (As_2O_4) (Sigma-Aldrich, #A6756), arsenic trioxide (As_2O_3) (Sigma-Aldrich, #17971), 3-bromopyruvate (3BP) (Sigma-Aldrich, #16490), iodoacetate (IA) (Sigma-Aldrich, #I2512), or koningic acid (KA) were added. After 24 hr, cell viability assays were carried out using MTT as previously described. IC_{50} values of drug concentrations were used unless otherwise stated.

Cell Viability Assays
For all cell lines, 5×10^3 cells/well were seeded in triplicate a 96-well plate and allowed to adhere for 24 hr. The following day, vehicle or KA was added to each well at the respective concentrations. After 24 hr, the media was aspirated and replaced with 100 μL phenol-red free RPMI-1640 (GIBCO) and 12mM 3-[4,5-Dimethylthiazol-2-yl]-2,5-diphenyltetrazolium (MTT) (Thermo Fisher Scientific, #M6494) was added to the cells. After 4 hr, the media containing MTT was aspirated and 50 μL DMSO was added to dissolve the formazan and read at 540nm. For HEK293T cells, 100 μL of SDS-HCl solution was added to each well and incubated for 4 hr at 37°C, followed by absorbance reading at 570nm.

Nutrient Supplementation in Media
For HCT116 and KA-sensitive cell lines, 5×10^3 cells/well were seeded in triplicate with complete RPMI-1640 media in 96-well plates and allowed to adhere for 24 hr. The following day, the respective treatment media was added in the absence or presence of KA at the cell lines' IC_{50}. MTT assays were carried out as previously described. All treatment media used were as follows: Low Glucose Media: RPMI-1640 with 0.5mM glucose (VWR, #97061-168), 10% heat-inactivated FBS, 100 U/ml penicillin and 100 μg/ml streptomycin with or without 3mM N-acetyl-cysteine (NAC) (Sigma-Aldrich, #A9165); Pyruvate Media: RPMI-1640 with 5mM pyruvate (Santa Cruz Biotechnology, #sc-208397), 10% heat-inactivated FBS, 100 U/ml penicillin and 100 μg/ml streptomycin with or without 3mM NAC; Lactate Media: RPMI-1640 with 5mM lactate (Santa Cruz, Biotechnology, #sc-253582), 10% heat-inactivated FBS, 100 U/ml penicillin and 100 μg/ml streptomycin with or without 3mM NAC; Serine Media: RPMI-1640 with 2mM additional serine (Amresco, #1B1103), 10% heat-inactivated FBS, 100 U/ml penicillin and 100 μg/ml streptomycin with or without 3mM NAC; Serine and Lactate Media: RPMI-1640 with 2mM additional serine, 5mM lactate, 10% heat-inactivated FBS, 100 U/ml penicillin and 100 μg/ml streptomycin; 3-phosphoglycerate (3PG) Media: RPMI-1640 with 2mM 3PG (Sigma-Aldrich, #P8877), 10% heat-inactivated FBS, 100 U/ml penicillin and 100 μg/ml streptomycin. Cells were grown at 37°C with 5% CO_2.

Tumor Cell Line Sensitivity Analysis
One-dose and five-dose screens were carried out by the Developmental Therapeutics Program (DTP) at the National Cancer Institute at National Institutes of Health (Bethesda, MD USA) on a panel of 59 independent cancer cell lines (Shoemaker, 2006). For the one-dose screen, 10 μM KA or 0.01% DMSO (Vehicle) was used and for the five-dose screen, concentrations of 0-100 μM KA or vehicle was used. The tumor cell lines were all grown in RPMI-1640 media containing 5% FBS and 2mM L-glutamine. Cells were seeded at 5,000 to 40,000 cells/well, depending on cell line doubling time, in 96-well plates containing 100 μL media and incubated at 37°C, 5% CO_2 for 24 hr before addition of KA. After 24 hr, two plates of each cell line were fixed in situ with TCA, to represent a measurement of the population of each cell line at the time of treatment. Following addition of vehicle or KA, the plates were incubated for 48 hr at 37°C, 5% CO_2. For adherent cells, cold TCA was added to fix the cells in situ and incubated for 60 min at 4°C. The supernatant was discarded and the plates were washed five times with tap water and left to air dry. Sulforhodamine (SRB) solution at 0.4% (w/v) in 1% acetic acid was added to each well, and plates were incubated for 10 min at room temperature. After staining, unbound dye was removed by washing five times with 1% acetic acid that the plates were left to air dry. Bound stain was solubilized with 10 mM trizma base, and the absorbance was read at 515nm. For suspension cells, the methodology remained the same except the assay was terminated by fixing settled cells at the bottom of the wells by adding 80% TCA. Time zero (Tz), control growth (C), treatment growth (Ti) with the drug at one and five concentration levels, percent growth inhibition (GI), and lethal concentrations (LC) were recorded. Data for the BT-474 cell line was added to the one-dose screen and five-dose screen.

GAPDH Activity Assay

Using a GAPDH Activity Assay Kit (BioVision, #K680), all cells were seeded at $1x10^6$ cells per 10cm plate with either 0.01% DMSO (Vehicle) or KA. After 24 hr, cells were lysed, NADH standard curve was made, and cells were measured at 450 nm in kinetic mode for 60 min at $37°C$ according to the manufacturer's instructions.

Lentiviral Transfection and Transduction

KAr-*GAPDH* cDNA was made by de novo gene synthesis (Origene) and subcloned into pLenti-C-Myc-DDK-IRES-Puro Expression Vector (KAr-GAPDH) (Origene/Blue Heron). HEK293T cells were seeded at $1x10^6$ cells per 10 cm plate in DMEM (GIBCO) supplemented with 10% Heat-Inactivated FBS, 100 U/mL penicillin, and 100 mg/ml streptomycin and allowed to adhere and reach 70% confluency. After, 6 μg KAr-GAPDH, (Origene/Blue Heron, cDNA: D14519.1) or empty vector (EV) (Origene, #PS100069), 4 μg PsPAX2 packaging vector (Addgene, #12260), and 2 μg PMD2.G envelope expressing plasmid (Addgene, #12259) were diluted into 600 μL jetPRIME buffer (Polyplus Transfection, #114-07) and vortexed. Next, 24 μL jetPRIME transfection reagent (Polyplus Transfection, #114-07) was added to the mixture, vortexed for 10 s, and centrifuged for 30 s. The mixture was left to incubate for 10 min at room temperature. Next, 600 μL of the transfection mix was added to each plate dropwise into serum containing DMEM, evenly distributed, and incubated at $37°C$, 5% CO_2. The transfection medium was replaced with fresh medium after 4 hr and returned to the incubator for 24 hr. Virus was collected and filtered with 0.4 μm filter (VWR International). HCT116 cells were seeded at 50% confluency per 10 cm plate in RPMI-1640 (GIBCO) supplemented with 10% Heat-Inactivated FBS, 100 U/mL penicillin and 100 mg/ml streptomycin and allowed to adhere overnight. The next day, virus-rich media was added to cells (1:1 with fresh RPMI-1640 media) for 24 hr. After, virus-rich media was removed and cells were plated with fresh RPMI-1640 media. HEK293T and HCT116 cells were incubated with 1 μg/ml puromycin for 48 hr and EV and KAr-GAPDH expressing HEK293T and HCT116 cells were verified by western blotting.

Immunoblotting

Samples were homogenized in 200 μL 1X RIPA buffer (VWR International) supplemented with 100 μM phenylmethylsulfonyl fluoride (PMSF), 2 μg/μl aprotinin, 5 μg/ml pepstatin, 1X phosphatase inhibitor cocktail, and 2 mM Dithiothreitol (DTT). And centrifuged at 14,000 rpm for 30 min at $4°C$. The supernatant was transferred to a clean tube and a Bradford Assay (Bio-Rad) was carried out to quantify protein concentration. Protein samples were loaded onto TGX stain-free precast gels (Bio-Rad) and transferred to polyvinylidene difluoride (PVDF) membranes. Membranes were blocked in 5% dry non-fat milk in TBST and incubated with anti-GAPDH (Abcam, #ab9485) 1:2500 in 5% BSA in TBST and anti-Actin 1:2000 (Thermo Scientific, #MA5-15739) in 5% dry non-fat milk in TBST. Horseradish peroxidase-conjugated anti-mouse (Rockland, #610-1302) and anti-rabbit (Rockland, #611-1302), 1:2000, were used as secondary antibodies. Chemiluminescent signals were detected with Clarity Western ECL Detection Kit (Bio-Rad, #1705061) and imaged using the ChemiDoc Touch Imaging System (Bio-Rad).

Culture and Isolation of Koningic Acid from *Trichoderma virens*

Trichoderma virens (G-4) (ATCC, MYA-297) was cultured aerobically at $26.8°C$ for 5 days on potato dextrose agar (Fisher scientific, #DF0013-17-6) plates (25 cm). Tween-20 (0.1% in H_2O, 15 mL) was added to each plate and spores were scraped off the surface of the agar and fungal tissue using a cell spreader. The concentration of spore suspensions was determined by counting spores using a hemacytometer. Then, 1 L of liquid medium in a 2 L Erlenmeyer flask was inoculated with $1x10^6$ spores mL^{-1}. The culture broth consisted of malt extract medium containing 3% malt extract (BD Biosciences, #211677), 2% glucose (VWR, #97061-168), and 0.1% peptone (BD Biosciences, #211677). Liquid cultures were placed at $25°C$ with shaking at 200 rpm for 7 days.

After 7 days, liquid fungal cultures including fungal tissue and media were frozen using a dry ice acetone bath, and lyophilized. The lyophilized residues were extracted with 500 mL of methanol (Fisher Scientific, #A452) (containing 0.2% acetic acid (Fisher Scientific, #A38-500)) for 3.5 hr with vigorously stirring. Extracts were filtered over cotton, evaporated to dryness, and stored in 8 mL vials.

Isolation and Purification of Koningic Acid

Methanol extracts derived from 1 L cultures were fractionated using large-scale reverse-phase flash chromatography on a Teledyne ISCO CombiFlash chromatography system with a Teledyne C18 gold (100 g) column with acetonitrile (organic phase) and 0.1% acetic acid in water (aqueous phase) as solvents at a flow rate of 60 mL/min. A linear ramp from 0% organic to 100% organic over 30 min was used and fractions containing KA were collected, evaporated to dryness, and transferred to 8 mL glass vials. Then, KA was dissolved in a minimal volume of methanol and further purified via semi-preparative HPLC using an Agilent XDB C-18 column (25 cm x 10 mm, 5 μm particle diameter) acetonitrile (organic phase) and 0.1% acetic acid in water (aqueous phase) as solvents at a flow rate of 3.6 mL/min. A solvent gradient scheme was used, starting at 5% organic for 3 min, followed by a linear increase to 100% organic over 27 min, holding at 100% organic for 5 min, then decreasing back to 5% organic over 0.1 min, and holding at 5% organic for the final 4.9 min, for a total of 40 min. Fractions containing pure KA were collected, evaporated to dryness, and transferred to 8 mL glass vials and stored at $-20°C$.

U-^{13}C-Glucose Stable Isotope Labeling

All cells (300,000 cells/well) were plated in a 6-well plate and allowed to adhere to the plate for 24 hr. Cells were then treated with either vehicle or KA for 6 hr, then replaced with RPMI-1640 media containing 11mM $U^{13}C$-glucose (Cambridge Isotope Laboratories, #CLM-1396) and vehicle or KA for 0-24 hr. Metabolites were then extracted.

CellPress

Metabolite Extraction

Metabolite extraction and subsequent Liquid-Chromatography coupled to High Resolution Mass Spectrometry (LC-HRMS) for polar metabolites of each cell line was carried out using a Q Exactive Plus as previously described (Liu et al., 2014a, 2014b). For culture from adherent cell lines, media was quickly aspirated. Next, 1 mL of extraction solvent (80% methanol/water) cooled to $-80°C$ was added immediately to each well and the plates were then transferred to $-80°C$ for 15 min. After, the plates were removed and the cells were scraped into the extraction solvent on dry ice. For tissue, the sample was homogenized in liquid nitrogen and then 5 to 10 mg was weighed in a new Eppendorf tube. Ice-cold extraction solvent (200 μl) was added to each tissue sample and homogenized using a tissue homogenizer. The homogenate was incubated on ice for 10 min. For plasma or media, 20 μL was transferred to a new Eppendorf tube containing 80 μL HPLC grade water. Next, 400 μL of ice-cold methanol was added to the sample for a final methanol concentration of 80% (v/v). Samples were incubated on ice for 10 min. For absolute quantitation of KA in plasma, 0-10 μM KA standards were added to extraction solvent before centrifugation. All metabolite extractions were centrifuged at 20,000 g at 4°C for 10 min. Finally, the solvent in each sample was evaporated using a speed vacuum for metabolite analysis. For polar metabolite analysis, the cell metabolite extract was first dissolved in 15 μL water, followed by dilution with 15 μL methanol/acetonitrile (1:1 v/v) (optima LC-MS grade, Fisher Scientific, methanol, #A456; acetonitrile, #A955). Samples were centrifuged at 20,000 g for 10 min at 4°C and the supernatants were transferred to LC vials. The injection volume for polar metabolite analysis was 5 μl.

Liquid Chromatography

An XBridge amide column (100 × 2.1 mm i.d., 3.5 μm; Waters) was employed on a Dionex (Ultimate 3000 UHPLC) for compound separation at room temperature. Mobile phase A is water with 5mM Ammonium Acetate, pH 6.9, and mobile phase B is 100% Aceto-nitrile. The gradient is linear as follows: 0 min, 85% B; 1.5 min, 85% B; 5.5 min, 35% B; 10 min, 35% B; 10.5 min, 35% B; 10.6 min, 10% B; 12.5 min, 10% B; 13.5 min, 85% B; and 20 min, 85% B. The follow rate was 0.15 ml/min from 0 to 5.5 min, 0.17 ml/min from 6.9 to 10.5 min, 0.3 ml/min from 10.6 to 17.9 min, and 0.15 ml/min from 18 to 20 min. All solvents are LC-MS grade and purchased from Fisher Scientific.

Mass Spectrometry

The Q Exactive Plus MS (Thermo Scientific) is equipped with a heated electrospray ionization probe (HESI) and the relevant parameters are as listed: evaporation temperature, 120°C; sheath gas, 30; auxillary gas, 10; sweep gas, 3; spray voltage, 3.6 kV for positive mode and 2.5 kV for negative mode. Capillary temperature was set at 320°C, and S lens was 55. A full scan range from 70 to 900 (m/z) was used. The resolution was set at 70,000. The maximum injection time was 200 ms. Automated gain control (AGC) was targeted at 3×10^6 ions. For targeted MS/MS analysis of KA, the isolation width of the precursor ion was set at 1.5 (m/z), high energy collision dissociation (HCD) was 35%, and max IT was 100 ms. The resolution and AGC were 70,000 and 200,000 respectively.

Peak Extraction and Data Analysis

Raw data collected from LC-Q Exactive Plus MS was processed on Sieve 2.0 (Thermo Scientific, https://www.thermofisher.com/order/catalog/product/IQLAAEGABSFAHSMAPV). Peak alignment and detection were performed according to the protocol described by Thermo Scientific. For a targeted metabolite analysis, the method ''peak alignment and frame extraction'' was applied. An input file of theoretical m/z and detected retention time of 197 known metabolites was used for targeted metabolite analysis with data collected in positive mode, while a separate input file of 262 metabolites was used for negative mode. m/z width was set to 10 ppm. The output file including detected m/z and relative intensity in different samples was obtained after data processing. If the lowest integrated mass spectrometer signal (MS intensity) was less than 1000 and the highest signal was less than 10,000, then this metabolite was considered below the detection limit and excluded for further data analysis. If the lowest signal was less than 1000, but the highest signal was more than 10,000, then a value of 1000 was imputed for the lowest signals. Mass isotopomer distributions (MID) were calculated and samples were normalized by comparing the ratio of glucose-derived labeled metabolites to unlabeled metabolites within each sample. Quantitation and statistics were calculated using Microsoft Excel and GraphPad Prism 6.0.

Kinetic flux profiling

The time-dependent lactate labeling pattern was modeled as with the following equation:

$$\frac{[X^*]}{X^T} = 1 - e^{-\frac{f_X}{X^T}t},$$

in which $[X^*]$ is the concentration of labeled lactate, X^T is the total concentration (both labeled and unlabeled) of lactate, f_X is the lactate production flux. This model was fit to lactate MIDs using the fit() function in MATLAB to determine relative lactate production fluxes. Relative lactate pool sizes were estimated from MS signal intensities.

Thermodynamic and Kinetic Analysis

Mathematical model of glycolysis downloaded from the BioModels Database repository (EMBL-EBI, http://www.ebi.ac.uk/biomodels-main/, MODEL1504010000) was first translated to C++ code using the SBML translator module in the Systems Biology

Workbench (http://sbw.sourceforge.net/) (Sauro et al., 2003) then simulated using the ODE solver gsl_odeiv2_step_msbdf in the GNU Scientific Library (Free Software Foundation, http://www.gnu.org/software/gsl/). FCC of an enzymatic step was computed by replacing V_{max} of the enzyme with $1.01V_{max}$ and $V_{max}/1.01$ while keeping all other parameters fixed, computing the corresponding steady state lactate fluxes (f_{Lac}), then estimating FCC accordingly: $FCC = \frac{\log f_{Lac}(1.01V_{max}) - \log f_{Lac}\left(\frac{V_{max}}{1.01}\right)}{2 \log 1.01}$. ΔGs were calculated from standard reaction free energies and steady state concentrations of the metabolites. Extent of the Warburg Effect was tuned by increasing V_{max}s of the glycolytic enzymes GLUT, HK, PFK, PGK, MCT from 0.1 to 10-folds of their original values and decreasing V_{max} of PDH from 10 to 0.1 folds of its original value simultaneously. Extent of the Warburg Effect was quantified by ratio of lactate production flux to oxidative phosphorylation flux.

Integrative Analysis of Drug Response and Multi-omics Data
All correlations were carried out using pearson or spearman correlations to GI_{50} values of KA to each of the 59 cell lines tested from the NCI-60 cell line panel using GraphPad Prism 6.0 or R Statistical Programming (The R Foundation, https://www.r-project.org/). Metabolic consumption and excretion rates from NCI-60 cell line panel were acquired from Jain et al. (2012). Cell size and doubling time were acquired from Dolfi et al. (2013). Gene expression analyses were completed by manually dividing the 59 cell lines tested with KA into two groups (KA-resistant and KA-sensitive) based on the distribution of GI_{50} values. Gene set enrichment analysis (GSEA) was then performed (The Broad Institute, http://software.broadinstitute.org/gsea/index.jsp) using all of the genes for differential expression analysis between KA-sensitive and KA-resistant cell lines. For protein expression analyses the efficacy of KA (in terms of GI50) were plotted against the absolute protein quantification of glycolytic genes in the NCI-60 cell line panel. Protein quantification data was obtained from Gholami et al. (2013) and genes were filtered and mapped to their KEGG biochemical pathways as previously described in Madhukar et al. (2015). P values, R^2, Pearson correlation values were calculated using the cor.test function within R. Mutation and copy number alterations (CNAs) were obtained from cBioPortal (http://www.cbioportal.org) for Cancer Genomics. Random distributions for the Q-Q plots were generated by permuting the original data 1000 times and calculating Spearman correlation coefficients accordingly. Error bars on the Q-Q plots represent for standard deviation of the quantiles of the 1000 random distributions. Drug activity z-scores of the targeted therapies calculated from their GI_{50} values on the NCI-60 cell line panel were available from CellMiner (National Cancer Institute, https://discover.nci.nih.gov/cellminer/). ROC curves were created for the targeted therapies using the perfcurve() function in MATLAB (MathWorks, https://www.mathworks.com/product/matlab.html), by labeling the cell lines according to presence of the genomic feature targeted and using drug activities as predictive scores. For KA, cell lines were labeled 'high' or 'low' based on whether the glucose or lactate flux in this cell line is higher or lower than the median value among all cell lines and ROC curves were created similarly.

Koningic Acid Docking to GAPDH
The virtual compound screening ZINC Database (http://zinc.docking.org) was used to obtain a ready-to-dock format (mol2) of KA (ZINC 15272438) (Irwin and Shoichet, 2005; Irwin et al., 2012). Next, docking between KA and the human GAPDH structure was performed using molecular docking on the Swiss Dock server using default settings (http://www.swissdock.ch) (Grosdidier et al., 2011). Since previous studies have already shown that the epoxide group of KA interacts with GAPDH active site cysteine 152 via alkylation, the highest scoring binding model with this interaction was used to infer the drug docking (Sakai et al., 1988, 1991). The 3-D structure of the docked model was analyzed using UCSF Chimera 1.10.2 (http://www.rbvi.ucsf.edu/chimera) (Pettersen et al., 2004). Amino acid hydrophobicity was assigned to the structure as an attribute in Chimera with a pre-defined hydrophobicity scale (Kyte and Doolittle, 1982).

GAPDH Protein Multiple Sequence Alignment Comparisons
All multiple sequence alignments were carried out using Clustal Omega http://www.ebi.ac.uk/Tools/msa/clustalo/) (Sievers et al., 2011). For phylogenetic analyses, outputs from Clustal Omega were used and inputted into Clustal W2-Phylogeny (http://www.ebi.ac.uk/Tools/phylogeny/simple_phylogeny/) (Larkin et al., 2007) to generate a phylogenetic tree from the homology alignment. Percent Identity Matrices were calculated based on the data output from Clustal W2-Phylogeny.

Analysis of Metabolomics Data
GENE-E and Morpheus software were used for hierarchal clustering and heatmap generation (The Broad Institute, https://software.broadinstitute.org/GENE-E/index.html). For hierarchal clustering, spearman correlation parameters were implemented for row and column parameters, with the exception of putative GAPDH drug response data, in which hierarchal clustering for row parameters only was used. Quantile normalization was used to normalize the data, with the exception of glycolysis data in HCT116 cells, in which and $\log_2$ normalization was used.

For pathway enrichment analyses, MetaboAnalyst 3.0 was used (http://www.metaboanalyst.ca/faces/home.xhtml) (Xia et al., 2015). To do this, HMDB IDs from the metabolites that were significantly enriched in their respective treatment groups (greater than $\pm \log_2(2)$ fold change with a $p < 0.05$) were inputted. The pathway library that was chosen was *Homo sapiens* and Fishers' Exact test was the method employed for over-representation analysis. For pathway topology analysis, relative betweenness centrality was chosen as the node importance measure.

Paraffin Embedding and Immunohistochemistry

All paraffin embedding, tissue sectioning, and immunohistochemical (IHC) staining was carried out by Duke University Pathology Research Histology and Immunohistochemistry Laboratory shared resource facility. For tissue embedding and sectioning, previously established protocols were followed (Fischer et al., 2008a). For hematoxylin and eosin (H&E) staining of tissue sections, standard protocols were used (Fischer et al., 2008b). For Ki67 staining for cell proliferation, Ki67 was detected by biotinylated goat anti-rabbit 1:300 (Thermo Scientific,# BA-1000) and the ABC Elite (Vector, #PK-7100). For GAPDH staining to detect GAPDH localization, GAPDH was detected by the anti-rabbit HQ 1:200 (Abcam, #760-4815) and the anti-HQ system (Roche/Ventana, #760-4820). All slides were observed and photographed under the microscope.

To quantify Ki-67 staining, ImageJ (National Institute of Health, https://imagej.nih.gov/ij/index.html) was used. To do this, a threshold was set (8-Bit Auto Threshold) until all the stained areas were selected. Next, specific parameters were chosen for measurements (area, min & max gray value, area fraction, limit to threshold). After, intensity measurements were performed and output was area. The areas were compared to the background to achieve percentage of staining.

QUANTIFICATION AND STATISTICAL ANALYSIS

Unless otherwise noted, all error bars were reported ± SEM with n = 3 independent biological measurements and statistical tests resulting in p value computations were computed using a Student's t test two tailed. Tumor volumes in the animal studies were analyzed by 2-way ANOVA of time matched values, followed by Bonferroni multiple comparison test. All statistics were computed using GraphPad Prism 6 (GraphPad, http://www.graphpad.com/scientific-software/prism/).

DATA AND SOFTWARE AVAILABILITY

Metabolomics data have been deposited to Mendeley Data and are available at http://dx.doi.org/10.17632/wmk2prwynj.1.